Materials Science & Engineering A 957 (2026) 149883

Contents lists available at ScienceDirect

Materials Science & Engineering A

journal homepage: www.elsevier.com/locate/msea

Dislocation-blocking enhancement mechanism in monolayer fullerene/copper composites

Qing Peng [a,b,c,*,1], Yuqiang Zhang [b,d,e,1], Gen Chen [b,d], Zeyu Huang [b,d], Xintian Cai [f,g,**], Wenhan Zeng [e], Wenbin Zhong [e], Zhongwei Hu [d,***], Xiao-Jia Chen [c], Xiangqian Jiang [e]

[a] Power and Mechanical Engineering, Wuhan University, Wuhan, 430072, China
[b] State Key Laboratory of Nonlinear Mechanics, Institute of Mechanics, Chinese Academy of Sciences, Beijing, 100190, China
[c] School of Science, Harbin Institute of Technology, Shenzhen, 518055, China
[d] Institute of Manufacturing Engineering, Huaqiao University, Xiamen, China
[e] EPSRC Future Metrology Hub, Centre for Precision Technologies, School of Computing and Engineering, University of Huddersfield, UK
[f] School of Mechanical Engineering, Hubei University of Technology, Wuhan, 430068, China
[g] Hubei Key Laboratory of Modern Manufacturing Quality Engineering, Wuhan, 430068, China

ARTICLE INFO

Keywords:
Monolayer fullerene
Copper composites
Dislocation-blocking
Interface plasticity
Molecular dynamics

ABSTRACT

The emerging monolayer fullerene (M-C_{60}) offers exceptional multifunctional properties, yet its role in reinforcing copper via dislocation-blocking remains unclear. Using molecular dynamics nanoindentation simulations, we compare single-crystal Cu, graphene/Cu, and M-C_{60}/Cu in surface-coated and embedded configurations. Key findings demonstrate that M-C_{60} coating enhances hardness by 24.2% via its sp^2-sp^3 hybrid structure leading to stair-rod/Hirth dislocation multiplication and carbon-chain formation, outperforming graphene's sp^2-based mechanisms. Embedded M − C_{60} absorbs and reflects mobile dislocations, reducing Hirth/Stair-rod dislocations by 54.1% and 16.7% and thereby improving ductility. Compared to graphene, M-C_{60} exhibits a 26.3% higher interfacial bonding-site density and superior stress buffering, enabling more versatile tuning of strength–ductility tuning. Strain-rate studies reveal that M-C_{60}/Cu retains hardness by resisting brittle fracture and sustaining dislocation loop formation, unlike graphene coatings that fail catastrophically. Elevated-temperature tests show that M-C_{60} coatings uniquely sustain or increase dislocation density due to strong Cu–C bonding and rough surface morphology, while graphene/Cu softens through dislocation annihilation and reduced twinning. In addition, the hardness-enhancement and dislocation-blocking mechanisms of M-C_{60} are intrinsic to the material and are not attributable to the indenter characteristics. This work establishes a dislocation-blocking design framework for metal matrix composites, resolving the longstanding strength-ductility trade-off through rational 2D/metal interface engineering.

1. Introduction

Two-dimensional (2D) nanomaterials, including graphene, molybdenum disulfide, tungsten diselenide, and hexagonal boron nitride, are characterized by their unique structure and exhibit outstanding mechanical [1,2], electrical [3,4], and thermal properties [5,6], which makes them well-suited for advanced applications in the aerospace, semiconductor, and electronics industries [7]. Recently, a novel all-carbon 2D material, monolayer quasi-hexagonal phase fullerene (M-C_{60}), was synthesized [8]. M-C_{60} features a planar topological structure formed by covalent bonds between C_{60} cluster cages [9,10]. This sp^2-sp^3 hybrid structure [11] provides M-C_{60} with unique mechanical flexibility, high electron mobility, and significant surface area, making it suitable for diverse electronics, energy storage, catalysis, and biomedicine applications. M-C_{60} exhibits high electron mobility in electronics, making it suitable for transistors and sensors [12].

* Corresponding author.
** Corresponding author.
*** Corresponding author.
E-mail addresses: pengqing@whu.edu.cn (Q. Peng), caixintian@hbut.edu.cn (X. Cai), huzhongwei@hqu.edu.cn (Z. Hu).
[1] These authors contributed equally to this work and share first authorship.

https://doi.org/10.1016/j.msea.2026.149883
Received 19 August 2025; Received in revised form 23 January 2026; Accepted 2 February 2026
Available online 17 February 2026

Additionally, its semiconducting properties are advantageous in manufacturing integrated circuits [13]. From a chemical perspective, M-C_{60}'s high surface area to volume ratio is beneficial for applications in energy storage and catalysis [14]. Its unique structure also allows adding functional groups, enabling property modifications tailored to specific applications. Mechanically, the flexibility of the two-dimensional material imparts a ductility akin to graphene, which can withstand large deformations without breaking [15]. This property makes it useful for manufacturing lightweight composites in the aerospace and automotive industries.

Integrating 2D carbon-based materials with substrates to develop nanocomposites has shown significant effectiveness in graphene-based composites. For example, carbon-based materials (graphene sheets, single-walled carbon nanotubes, multi-walled carbon nanotubes) have been used as reinforcing agents in epoxy resin nanocomposites, where the performance of graphene sheets was superior to that of carbon nanotubes [16]. Graphene also improves thermal conductivity in polymer composites due to the large contact area and interfacial solid interactions of graphene [17]. MD (molecular dynamics) simulations revealed graphene's role in enhancing polymer composites' mechanical properties [18]. However, metals have excellent specific strength, higher working temperature, and better corrosion resistance, and they are emerging as viable alternatives to polymers. Therefore, metal matrix composites (MMCs) are increasingly becoming the focus of academic research [19–21]. In 2013, graphene-metal nanosheet composites were successfully synthesized, demonstrating the mechanical enhancement benefits of graphene in MMCs [22]. Despite graphene's success in enhancing strength, its limited interfacial bonding sites often lead to premature failure under cyclic loading due to insufficient dislocation accommodation [23]. This critical limitation necessitates exploring 2D reinforcements with enhanced interfacial activity to achieve simultaneous strength-ductility optimization. Copper is the primary material used for microcircuit interconnects in large-scale integrated circuits within semiconductor devices [24–26]. Gr is being considered to strengthen copper due to its insufficient strength [27,28]. However, the study of copper/graphene composites indicated that the effect of periodic graphene strengthening may be overestimated [29]. Monolayer fullerene, as an allotrope of graphene, has been extensively examined for its inherent properties, such as its anisotropic optical properties [30,31], mechanical properties [32,33], thermoelectric performance [34], catalytic activity [14], and thermal stability [35]. Despite the promising properties of M-C_{60}, how M-C_{60}'s hybrid bonding structure governs dislocation nucleation and propagation in Cu matrix remains unexplored—a knowledge gap critical for designing damage-tolerant composites. Thus, investigating the mechanical behavior of M-C_{60}/metal composites is beneficial for discerning their prospective applications. MD is an effective method for studying the mechanical properties of materials [36], as it allows direct observation and analysis of material structure and movement at the atomic and molecular levels. It is beneficial for understanding the microscopic mechanisms of materials under mechanical effects, such as dislocation movement and phase change, and it provides theoretical guidance for the practical application of materials [37,38]. Moreover, Cu-C systems, including Cu/graphene and Cu/CNT, have been systematically studied using MD simulations [39–42].

This study systematically investigates the mechanical properties of M-C_{60}/Cu composites (including coating and embedding structures) under nanoindentation using molecular dynamics simulations and compares them with Cu and graphene/Cu composites. By examining the differences in force, dislocation, stress distribution and different conditions (strain rate, temperature and indenter geometries) among various composites, we can better understand the reinforcement mechanism of M-C_{60}. This research aims to provide insights for designing high-performance composites for aerospace, electronics, and other high-stress applications.

2. Model and methods

2.1. Molecular dynamics model

Molecular dynamics simulations were conducted using LAMMPS (a large-scale atomic/molecular massively parallel simulator) [43], and the MD model was represented in Fig. 1. The initial crystalline cell of M-C_{60} is shown in the red rectangular area in Fig. 1(a), with lattice constants a = 0.92 nm, b = 1.60 nm, and c = 1.22 nm [8]. C_{60} structures form a regular hexagonal pattern. The sides of the hexagon parallel to the x-axis are labeled 'armchair', and those parallel to the y-axis are called 'zigzag' [44,45], as depicted in Fig. 1(b). M-C_{60}/Cu and Gr/Cu composites comprise single-crystal copper, Gr, and monolayer quasi-hexagonal phase fullerene, respectively, as demonstrated in Fig. 1 (c). In the Cartesian coordinate system, the crystal orientation of Cu is defined as [100], [010], and [001]. Its zigzag and armchair shapes align with the X and Y axes. M-C_{60} and Gr are set on the Cu (001) surface, referred to as the coating. M-C_{60} and Gr are interposed within Cu, referred to as the embedding. The distance between M-C_{60} and the Cu (001) surface was fixed at 0.72 nm, and the setup of Gr is the same. To minimize interfacial strain, the in-plane lattice parameters of the copper substrate and the 2D reinforcement (Gr or M-C_{60}) were matched by constructing commensurate supercells. The mismatch ratio δ was defined as:

$$\delta = \frac{\left|a_{Cu}^{(n)} - a_{2D}^{(m)}\right|}{a_{Cu}^{(n)}} \times 100\% \quad (1)$$

where $a_{Cu}^{(n)}$ and $a_{2D}^{(m)}$ are the in-plane lattice lengths of the $n \times n$ copper surface unit cell and the $m \times m$ 2D layer supercell, respectively. The goal was to find integer n and m pairs that minimized δ while keeping the supercell dimensions close to the target simulation size. In this study, an 84 × 84 Cu (001), a 33 × 19 M-C_{60}, and a 122 × 71 Gr unit cell were constructed. This configuration yielded mismatch rates of 0.006% and 0.071% in the X-direction and 0.059% and 0.071% in the Y-direction, substantially reducing lattice discrepancies. A diamond, composed of a hemispherical and cylindrical shape with a radius of 4 nm, was selected as the material for the indenter. The specific parameters of the simulation model are shown in Table 1. In terms of boundary conditions, periodic boundary conditions were implemented along both the X and Y directions to simulate an infinite lattice in these directions, while fixed boundary conditions were applied along the Z direction to replicate the real nanoindentation scenario. All models underwent relaxation after energy minimization, followed by indentation simulations under NVE conditions. During the indentation simulation, the indenter was placed directly above the geometric center of the model. The indenter was lowered at a velocity of 100 m/s to reach a loading depth of 4 nm before being unloaded at an identical rate.

2.2. Interatomic potentials

The interactions of C-C atoms in the M-C_{60} and Gr were depicted using the AIREBO (adaptive intermolecular reactive empirical bond order) potential, with a cut-off value of 0.2 nm [46–48]. The Tersoff potential characterized the interactions among carbon atoms in the indenter, and the EAM (embedding atom method) [49–51] described interactions among copper atoms. The LJ (Lennard-Jones) potential was utilized to represent the interactions between Cu, M-C_{60}, Gr, and the indenter [52–54]. LJ potential parameters for Cu-C, C–C interaction can be listed in Table 2. To validate the compatibility of the AIREBO potential with M-C_{60}, the stretching simulations were performed along the X and Y axes, respectively, as illustrated in Fig. 1(b). The three-dimensional dimensions of the M-C_{60} were 30.26 nm × 30.40 nm × 1.22 nm, comprising 75,240 atoms. Periodic boundary conditions were implemented. The box size along the Z axis was set to 20 nm to

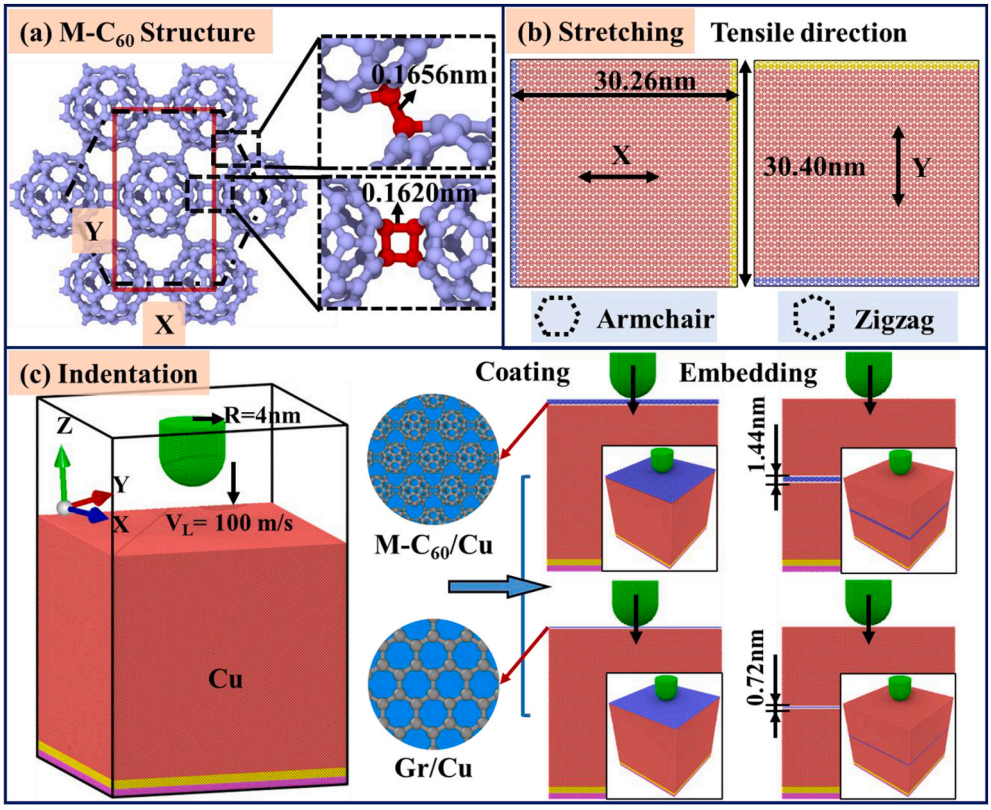

Fig. 1. The MD models in this study: **(a)** Monolayer quasi-hexagonal phase fullerene; **(b)** The stretching of M-C_{60} (X and Y direction); **(c)** Nanoindentation of Cu, M-C_{60}/Cu and Gr/Cu composites.

Table 1
Parameters employed in this study.

Parameter	Specimens:			Tools: Diamond
	Cu	M-C_{60}/Cu	Gr/Cu	
Dimensions (nm)	30.34 × 30.34 × 30.34			Radius: 4
Number of atoms	2370816	2375496	2377137	34060
Ratio (wt%/vol%)	0	0.62/4.03	0.28/1.14	
Time step (fs)	1.0			
Temperature (K)	100, 200, 300, 400, 500			
Depth (nm)	4			
Speed (m/s)	60, 80, 100, 120, 140, 250, 500, 750, 1000			

Table 2
Parameter for Lennard – Jones potential used the simulations [52–54].

Parameter	ε(eV)	σ(nm)
Cu-C	0.019996	0.3225
C-C	0.00286	0.347

minimize the periodicity effects in the Z direction optimally. Before the stretching process, energy minimization was initially undertaken via the conjugate gradient method with a 0.001 ps timestep. Then, the structures underwent equilibration in an NPT ensemble, maintaining a temperature of 300 K and zero pressure through a Nosé-Hoover thermostat for 200 ps. Finally, under NVT conditions, uniaxial uniform stretching was implemented on the X and Y axes at a strain rate of 0.005/ps until overall structural rupture. Detailed results and analysis are presented in Section 2.3.

The simulation results were analyzed by OVITO as the visualization tool [55]. The DXA (dislocation extraction algorithm) facilitated the detection of distinct dislocation lines and acquiring structural information [56]. The interaction behaviors between atoms were observed via atomic strain, while the motion of dislocations was monitored through the displacement vectors of atoms. The CNA (common neighbor analysis) discerned defective atoms, and the atomic von Mises strain was deployed to monitor inelastic deformations [20,57,58].

2.3. Stress-strain of stretching

Fig. 2 illustrates the stress(δ)-strain(ε) curves and shear strains corresponding to the fracture of M-C_{60} during its stretching along the X and Y axes. As can be inferred from Fig. 2(a), the stretching process is categorized into three stages: elastic, yield, and fracture. Initially, the stress-strain curve exhibits a linear relationship, indicating elastic deformation. Young's modulus was calculated as 146.13 GPa along the X direction and 127.70 GPa along the Y direction, demonstrating the material's anisotropy. In the absence of experimental values for comparison, confirming the precision of the results is difficult. However, the values are consistent with the elastic moduli reported in the literature [59,60,61]. As the strain increases, the material enters the yield stage, characterized by a deviation from linearity. The maximum yield stress was observed at 39.89 GPa for the X direction ($\varepsilon = 0.273$) and 22.92 GPa for the Y direction ($\varepsilon = 0.262$). The final stage is marked by a sudden drop in stress, indicating brittle fracture [11].

The fracture behavior showed a distinct anisotropy, with different fracture mechanisms along the X and Y directions. As shown in Fig. 2(b), horizontal C-C bonds broke first when stretched along the X direction. Along the Y direction, C-C bonds oriented at 60° to the horizontal ruptured initially. The formation of carbon chains post-fracture was similar to that observed in graphene under tension [40,62]. To assess the suitability of the AIREBO potential function, stress-strain data calculated using Density Functional Theory (DFT) and the Reactive Force-Field (ReaxFF) were compared, as shown in Fig. 2(a). Fig. 3 presents the calculated theoretical Young's modulus values from the elastic stage. All calculation methods showed a higher Young's modulus value along the

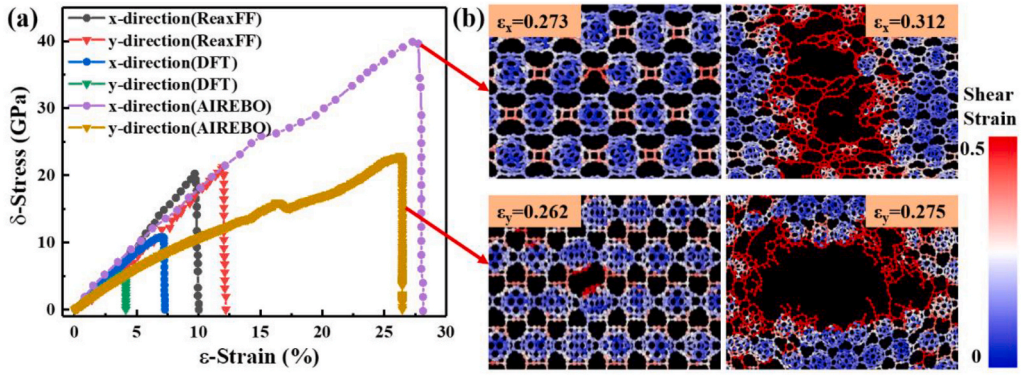

Fig. 2. The stretching of the M-C_{60} along the X and Y axes: **(a)** Stress(δ)-strain(ε) curves; **(b)** Shear strains corresponding to the fracture, with atoms colored according to their shear strain.

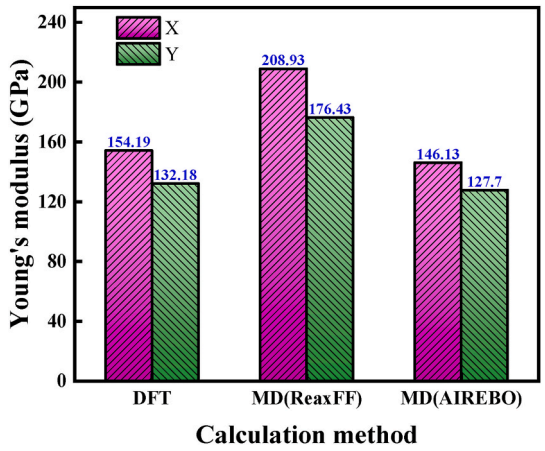

Fig. 3. The theoretical Young's modulus of the elastic stage calculated by different calculation methods, where pink and green represent the results of stretching along the X and Y directions, respectively. (For interpretation of the references to color in this figure legend, the reader is referred to the Web version of this article.)

X-axis than the Y-axis. The value calculated via ReaxFF deviates significantly from the DFT calculation (X_error:35.50%; Y_error:33.48%), whereas the AIREBO potential function calculations exhibit relatively more minor errors (X_error:5.23%; Y_error:3.39%). Despite the significant difference in temperature conditions between DFT calculations, which approximate results at near-zero base temperature, and MD simulations via the ReaxFF and AIREBO computed at 300K, M-C_{60} shows excellent thermal stability as supported by previous research [3]. Therefore, the results of the DFT calculations can be relied upon. In the second deformation stage, both DFT and ReaxFF calculations exhibit a short yield state before reaching their maximum tensile strength. In contrast, the AIREBO calculations exhibit a longer yield stage. The critical strain for the DFT and ReaxFF calculations in the X-direction (Y-direction) is 7.0% (4.1%) and 9.6% (11.9%), respectively, and the ultimate tensile stresses are 10.8 GPa (5.4 Gpa) and 21.7 GPa (20.4 GPa) respectively. The calculated differences can be attributed to the effects of the new sp^2-sp^3 hybrid structure.

3. Results and discussion

3.1. Load-depth relationship

Fig. 4(a) presents the load-depth (*P-h*) curves during the complete loading and unloading cycles of nanoindentations for Cu, M-C_{60}/Cu composites, and Gr/Cu composites. The curves reveal the effect of M-C_{60} (Gr) and its position on the distinct mechanical response of the synthesized composites. In nanoindentation, the fluctuation of load-depth curves is attributed to the material's plastic rearrangement and strain hardening [63]. Moreover, the *P-h* curves are compared with the curves calculated using the Hertzian theory. While experimental validation is desirable, current limitations in synthesizing M-C_{60}/Cu composites restrict direct experimental comparisons. Thus, Hertzian contact theory was used as a theoretical benchmark. Following the Hertzian contact theory, the correlation between P and h is delineated as follows [64]:

$$P = \frac{4}{3} E_r R^{1/2} h^{3/2} \tag{2}$$

in which E_r represents the equivalent elastic modulus, expressed as:

$$\frac{1}{E_r} = \frac{1-\gamma_{hkl}{}^2}{E_{hkl}} + \frac{1-\gamma_{2D}{}^2}{E_{2D}} + \frac{1-\gamma_i{}^2}{E_i} \tag{3}$$

where E_{hkl}, E_{2D} represent the Young's modulus of copper and M-C_{60}(Gr), respectively, while γ_{hkl}, γ_{2D} correspond to their respective Poisson ratios. E_i and γ_i denote the Young's modulus and Poisson's ratio of the indenter. Given that the indenter is treated as a rigid body in the simulation, E_3 is assumed to be infinite. For 2D materials, the in-plane Young's modulus [65] and Poisson's ratio [66] along an arbitrary direction can be expressed as:

$$\frac{1}{\mathrm{E}(\phi)} = S_{11}(\cos\phi)^4 + S_{22}(\sin\phi)^4 + (2S_{12}+S_{66})(\cos\phi)^2(\sin\phi)^2 \tag{4}$$

$$\gamma(\phi) = \frac{(S_{11}+S_{22}-S_{66})\sin^2\phi\cos^2\phi + S_{12}(\cos^4\phi+\sin^4\phi)}{S_{11}\cos^4\phi + S_{22}\sin^4\phi + (2S_{12}+S_{66})\sin^2\phi\cos^2\phi} \tag{5}$$

where ϕ is the angle between the crystallographic c-axis and the normal to the plane of interest. S_{ij} denotes the components of the elastic compliance matrix S, which is the inverse of the stiffness matrix C (i.e., $S = C^{-1}$).

When the loading is axisymmetric, the sheet is stretched radially in every azimuth. The usual trick is to average the compliance over 0-2π:

$$\frac{1}{\overline{E_{2D}}} = \frac{1}{2\pi}\int_0^{2\pi} \frac{1}{\mathrm{E}(\phi)} d\phi \tag{6}$$

$$\overline{\gamma_{2D}} = \frac{\int_0^{2\pi} \nu(\phi)\left[\frac{1}{E(\phi)}\right] d\phi}{\int_0^{2\pi}\left[\frac{1}{E(\phi)}\right] d\phi} \tag{7}$$

To convert an in-plane 2D Young's modulus to a 3D Young's modulus, divide by the nominal thickness d of the 2D layer:

$$E_{3D} = E_{2D}/d \tag{8}$$

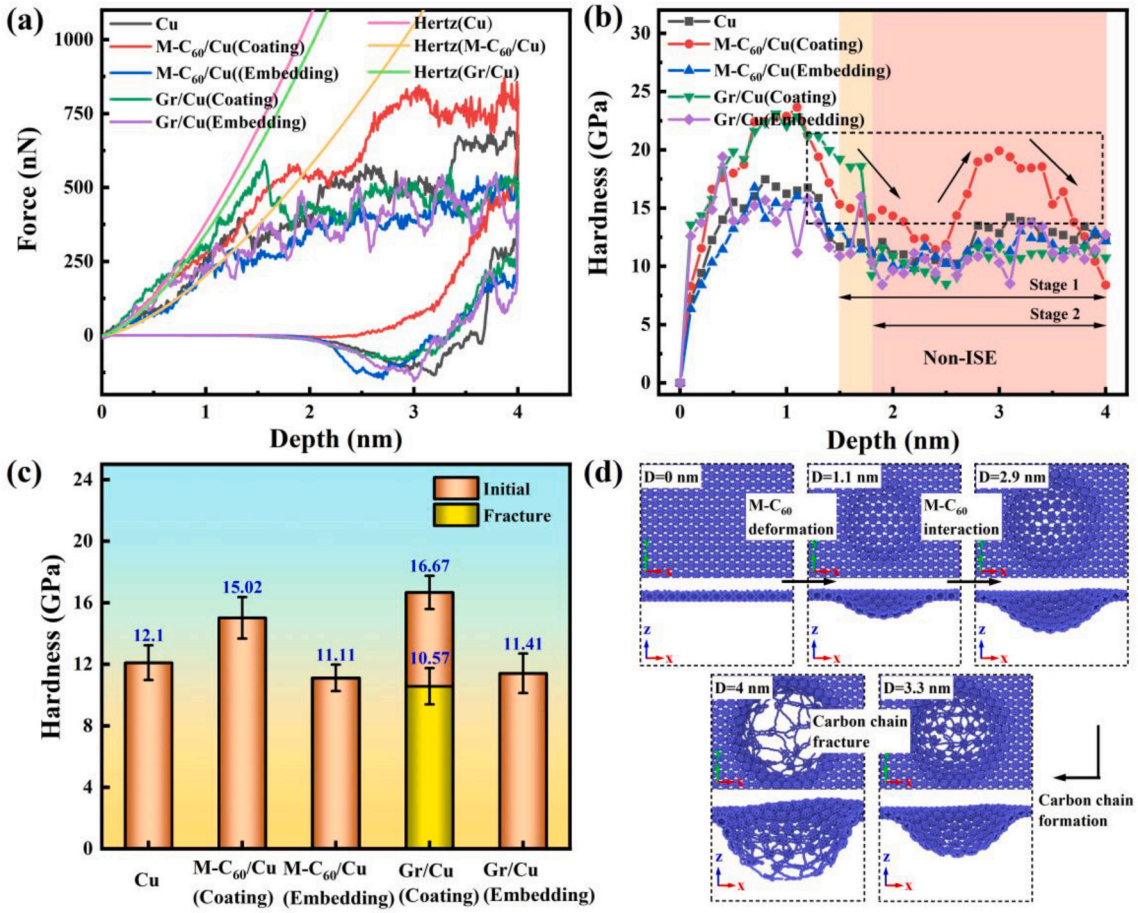

Fig. 4. Evolution of force **(a)** and hardness **(b)** with indentation depth for different materials: Cu-black; M-C_{60}/Cu (Coating)-red; M-C_{60}/Cu (Embedding)-blue; Gr/Cu (Coating)-green; Gr/Cu (Embedding)-purple; **(c)** Average hardness of non-ISE area for five materials, with yellow representing the hardness of Gr/Cu (Coating) after graphene breaks; (d) Evolution of M-C_{60} deformation with changing indentation depth. It should be noted that only Gr/Cu (coating) uses the dataset from the light-red region (Stage 2) to compute the corresponding average hardness. For all other materials, the dataset from the light-yellow region (Stage 1) is used to calculate the average hardness. (For interpretation of the references to color in this figure legend, the reader is referred to the Web version of this article.)

Poisson's ratio is dimensionless and therefore remains invariant when extended to three dimensions.

The elastic modulus and Poisson's ratio of different crystal planes of 3D materials [67,68] can be expressed as:

$$\frac{1}{E_{hkl}} = S_{11} - 2\left(S_{11} - S_{12} - \frac{1}{2}S_{44}\right)\left(l_1{}^2 l_2{}^2 + l_2{}^2 l_3{}^2 + l_1{}^2 l_3{}^2\right) \tag{9}$$

$$\gamma_{hkl} = -\frac{S_{12} + \left(S_{11} - S_{12} - \frac{1}{2}S_{44}\right)\left(l_1^2 m_1^2 + l_2^2 m_2^2 + l_3^2 m_3^2\right)}{S_{11} - 2\left(S_{11} - S_{12} - \frac{1}{2}S_{44}\right)\left(l_1^2 l_2^2 + l_2^2 l_3^2 + l_3^2 l_1^2\right)} \tag{10}$$

where, E_{hkl} and γ_{hkl} denote the Young's modulus and Poisson's ratio for the crystallographic plane (hkl). l_1, l_2, l_3 are the direction cosines of the loading direction (tension or compression) with respect to the crystal axes, satisfying

$$l_1 = \frac{h}{\sqrt{h^2+k^2+l^2}}, l_2 = \frac{k}{\sqrt{h^2+k^2+l^2}}, l_3 = \frac{l}{\sqrt{h^2+k^2+l^2}} \tag{11}$$

m_1, m_2, m_3 are the direction cosines of the transverse strain–measurement direction. They are orthogonal to the loading direction, so they satisfy

$$l_1 m_1 + l_2 m_2 + l_2 m_3 = 0 \tag{12}$$

The independent elastic constants of Cu, graphene, and monolayer fullerene (M-C_{60}) are listed in Appendix(Table A1).Therefore, the Hertzian theoretical curves of copper, M-C_{60}/Cu, and Gr/Cu composites are determined at E_r of 142.6, 126, and 62.57 GPa, respectively, with their elastic modulus and Poisson's ratio taken from Refs. [20,69]. Notably, in the initial stages of indentation, all materials exhibit elastic behavior. As the indentation depth increases, the materials transition to plastic deformation, characterized by a deviation from the theoretical Hertzian curve. The critical indentation depth, defined as the depth at which the material transitions from elastic to plastic deformation, is approximately 0.5 nm for Cu [70], 0.3 nm for the embedding composites of M-C_{60}/Cu and Gr/Cu. These values are consistent with theoretical predictions based on Hertzian contact mechanics. For coating composites, the response of M-C_{60}/Cu and Gr/Cu deviates from their Hertzian curve. However, the curve of M-C_{60}/Cu is in good agreement with the theoretical Hertzian curve of Cu, deviating at an indentation depth of 0.9 nm. The coating curve of Gr/Cu composites mirrors that of M-C_{60}/Cu composites and the critical indentation depth is 0.5 nm.

Furthermore, compared to copper (76 nN), the critical loads for the coating composites of M-C_{60}/Cu (253 nN) and Gr/Cu (168 nN) increased by 233% and 122%, respectively. Embedding in the copper matrix, the critical load decreases by 33% for M-C_{60}/Cu (38 nN). On the other hand, it increases by 25% for Gr/Cu (79 nN), which is attributed to the high strength of Gr. Overall, the peak load and corresponding indentation depth are higher for coating composites than pure copper and embedding composites, indicating enhanced load-bearing capacity. The enhancement effect of M-C_{60} is significantly higher than that of Gr.

Although the initial force of Gr/Cu (Coating) exceeds that in the M-C_{60}/Cu (Coating), then falls below that of copper. This difference is mainly attributed to M-C_{60} (Gr) and its position. It is also related to the fracture behavior of M-C_{60} (Gr). After retraction of the indenter, the minimal adhesion between the indenter and substrate can be observed in the coating, with embedding and single-crystal copper giving similar results. However, embedding significantly delays the rebound effect compared to single-crystal copper.

Fig. 4(b) depicts the indentation-hardness curves, revealing the responses of the five systems under plastic deformation conditions. The hardness values from nanoindentation in the plastically deformed state were ascertained by the Oliver-Pharr method [71]. The hardness value is equal to the quotient of the indentation load P (nN) to the projected contact area A_c (nm^2), as expressed in equation (13).

$$H = \frac{P}{A_c} \tag{13}$$

in which $A_c = \pi h(2r - h)$. And h represents the indentation depth, and r denotes the radius of the indenter.

The hardness of the five materials initially increases and then declines with increasing indentation depth, as shown in Fig. 4(b), which is attributed to the influence of indentation size effects [72]. The mean hardness value in the non-ISE region is taken as the material's intrinsic hardness to reflect the materials' true mechanical properties, as shown in Fig. 4(c). Gr/Cu (Coating) achieves a peak hardness of 16.67 GPa, 37.8% higher than pure Cu (12.1 GPa), but rapidly degrades to 10.57 GPa post-fracture due to graphene's brittle failure. The coating hardness of M-C_{60}/Cu, the second highest, is 15.02 GPa. Notably, the hardness of the M-C_{60}/Cu coating first decreases, then increases briefly before declining again. Initially, the drop in hardness is caused by deformation of the spherical C_{60}. It then recovers as interactions among M-C_{60} lead to the formation of carbon chains and finally diminishes again as these chains progressively fracture. The full evolution sequence is shown in Fig. 4(d). The hardness of Cu is 12.1 GPa. The hardness of the composite coated with only 0.62 wt% M-C_{60} is 24.2% higher than that of Cu. While the hardness of embeddings is the lowest, M-C_{60}/Cu and Gr/Cu exhibit hardnesses of 11.11 GPa and 11.41 GPa, respectively, which are 5.7% and 8.2% lower than Cu. During the loading process, the M-C_{60} and Gr directly contact the indenter, indicating initial deformation in these materials. As a spherical structure, fullerene exhibits significant load-bearing capacity [73], contributing to its high hardness. Graphene is stronger than fullerene, so its hardness is higher than fullerene in the initial period. When the Gr breaks, the Cu matrix is in contact with the indenter. In addition, partially broken carbon chains or carbon atoms are embedded into the copper matrix, as shown in Fig. 9(a4). Therefore, in this case, the overall hardness of the material is reduced.

Significant atomic displacement within the indentation area causes noticeable plastic deformation, as shown in Fig. 5. Using M-C_{60} and Gr as coatings results in significantly more plastic deformation than Cu, which exhibits more plastic deformation than when embedded (M-C_{60} and Cu). The behavior of plastic deformation corresponds to the hardness results. Embeddings show lower hardness as they absorb partially force when the load reaches the surfaces of M-C_{60} and Gr, thus alleviating accumulated stress at the tip of the indenter. The difference in hardness between M-C_{60}/Cu (Embedding) and Gr/Cu (Embedding) primarily results from the spherical fullerenes absorbing part of the force and deforming under load. At the same time, the force is transmitted to the spherical fullerenes—effective neutralization of reflected forces is shown in Fig. 8(c, e).

3.2. Ductility

Ductility serves as a key criterion for determining whether a crystal will lose its ability to undergo plastic flow as a result of rapid cleavage. It is often evaluated using the Pugh ratio [33], D = B/G, where B and G are the bulk and shear moduli, respectively. When D exceeds the critical threshold (approximately 1.75 for metals), the material is deemed ductile; when D falls below 1.75, it is considered brittle. In this study, we describe crystal ductility in the plastic-deformation regime by analogy to the Doerner–Nix function [74], as shown in Equation (14).

$$\frac{1}{D_r} = \frac{1}{D_{hkl}} + \left(\frac{1}{D_{2D}} - \frac{1}{D_{hkl}}\right)\exp(-\alpha(z/h)) \tag{14}$$

Here, D_{hkl} denotes the ductility of the substrate along the (hkl) crystal plane, while D_{2D} represents the ductility of the graphene or M-C_{60} layer. The parameter α is a dimensionless constant (set to 1 in this study), and h is the thickness of the two-dimensional material. The variable z specifies the position of the 2D layer within the substrate, taking a value of 0 when the layer lies at the surface and 1 when it is embedded in the bulk. For computational simplicity, the bulk modulus B and shear modulus G were obtained from the classical isotropic elastic contact theory [75].

$$B = \frac{E}{3(1-2\nu)}, G = \frac{E}{2(1+\nu)}. \tag{15}$$

Fig. 6 compares the Pugh ratios of five materials. Pure Cu shows a D of 1.86, indicating moderate ductility. The embedded M-C_{60}/Cu composite exhibits the highest D (3.48), signifying superior ductility, followed by embedded Gr/Cu with D = 2.65. These results demonstrate that embedding either M-C_{60} or graphene in the Cu matrix markedly improves ductility; the underlying mechanism is discussed in the dislocation analysis. In contrast, the coating configurations—M-C_{60}/Cu

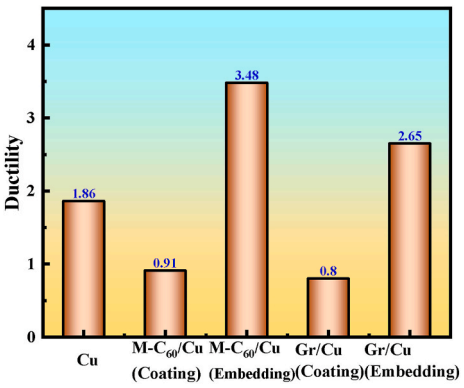

Fig. 6. Ductility of five materials: Cu; M-C_{60}/Cu (Coating); M-C_{60}/Cu (Embedding); Gr/Cu (Coating); Gr/Cu (Embedding).

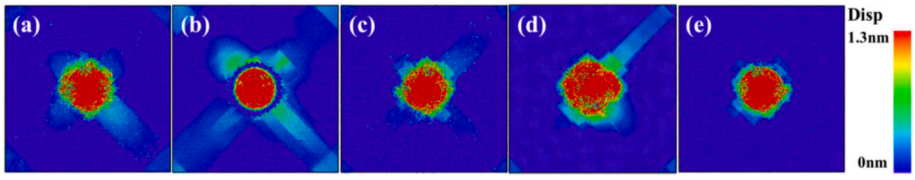

Fig. 5. Distribution of atomic displacements in the xy plane of the substrate during nanoindentation, with atoms colored according to their displacement: **(a)** Cu; **(b)** M-C_{60}/Cu (Coating); **(c)** M-C_{60}/Cu (Embedding); **(d)** Gr/Cu (Coating); **(e)** Gr/Cu (Embedding).

and Gr/Cu—display much lower D values of 0.91 and 0.80, respectively. When the 2D layer lies at the surface, applied loads are transmitted directly to the brittle M-C_{60} or graphene sheet, causing the composite to fail in a brittle manner.

In addition, it should be noted that in our MD nanoindentation simulations, dislocation analysis serves as another key metric: a higher density of mobile Shockley partials and fewer sessile Hirth or stair-rod dislocations indicate greater capacity for sustained plastic flow. While this approach does not measure ductility in the conventional tensile sense, it provides a consistent, mechanistically linked proxy for comparing systems within the same simulation framework.

3.3. Dislocations

The dislocation density increases with the indentation depth during the loading process, as shown in Fig. 7(a). Initially, the curves remain stable and at zero since the deformation of the workpiece is in the elastic stage. Subsequently, the dislocation densities of both Cu and coating increased rapidly while that of the embedding increased slowly. Compared with Cu, Cu surface-coated M-C_{60} or Gr produces more dislocation lines with increasing depth. Specifically, Gr coating results in higher dislocation densities than M-C_{60} coating prior to any fracture in Gr. The increase in dislocation density contributes to the strengthening of the material. When M-C_{60} and Gr are positioned centrally within the Cu matrix, the dislocation density is the lowest, improving the material's ductility. The lengths of various dislocation types at an indentation depth of 4 nm for the five materials are displayed in Fig. 7(b). Changes in total dislocation length correspond with trends in hardness. The increase in 1/6<110> stair rod and 1/3<100> Hirth dislocations is a primary reason for strengthening the material hardness. M-C_{60}/Cu (Coating) generates the highest number of dislocations, followed by single-crystal copper. The dislocation density in M-C_{60}/Cu (Coating) reaches 6.0 ×

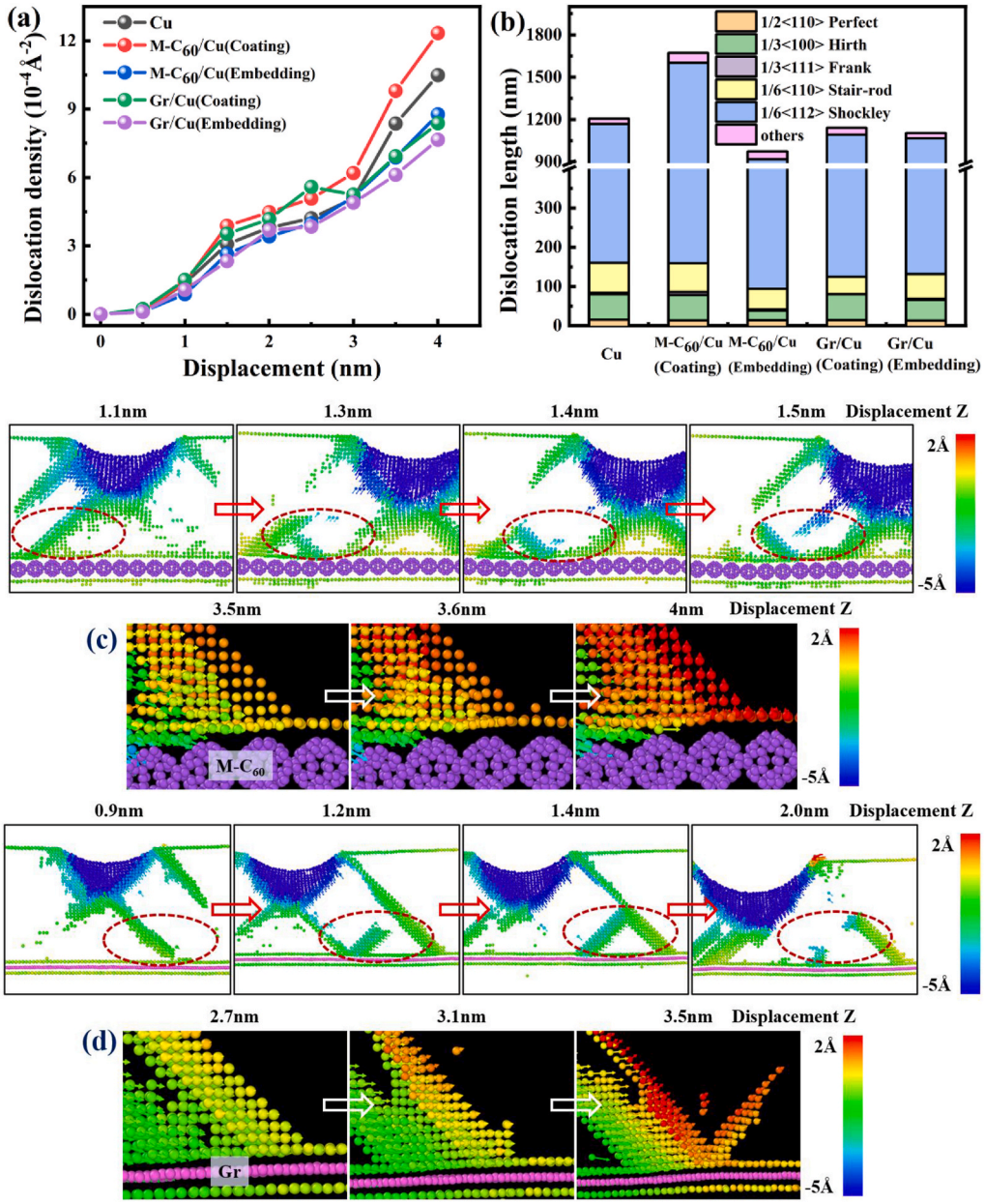

Fig. 7. (a) Variation of dislocation density with indentation depth; **(b)** Lengths of different types of dislocations inside the substrate; **(c–d)** Dislocation evolution of the embeddings at different indentation depths, with atoms colored according to their displacement in the Z direction. Special emphasis is placed on M-C_{60} and Gr, colored purple and pink, respectively. (For interpretation of the references to color in this figure legend, the reader is referred to the Web version of this article.)

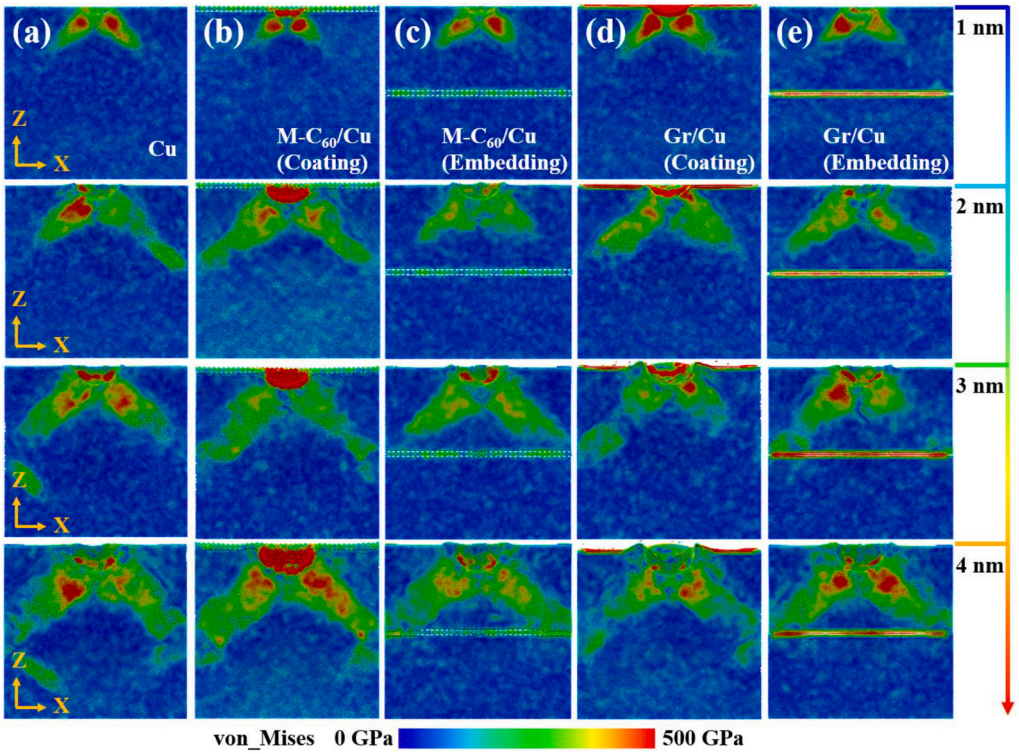

Fig. 8. Variation of von Mises stress in the xz plane for Cu, Coatings, and Embeddings at different indentation depths (d = 1, 2, 3, 4 nm), with atoms colored according to the von Mises stress values.

10^{16} m^{-2} at 4 nm depth, 39.5% higher than pure Cu (4.3×10^{16} m^{-2}), directly correlating with its 21.3% hardness enhancement. The dislocation lengths in Gr/Cu (Coating) and Gr/Cu (Embedding) are similar, resulting in nearly identical final hardness values. For M-C_{60}/Cu (Embedding), the lengths of the Hirth and stair-rod dislocations are reduced by 54.1% and 16.7%, respectively, compared to Gr/Cu (Embedding), resulting in the lowest hardness.

To further explore the causes of the significant reduction in dislocation density observed in the embedding during the loading process, the dislocation analysis (DXA) and atomic displacement map were performed, as depicted in Fig. 7(c and d). During the loading process, phenomena such as dislocation nucleation, slip, interaction, loop formation, shrinkage, and annihilation occur. In the initial stage, the surface of the workpiece undergoes slight deformation, producing shear strain that leads to two inclined slip planes (at a 45° angle to the surface) and dislocation prototypes. As strain consistently increases, dislocations rapidly move along the slip planes until they partially terminate at the surfaces of M-C_{60} and Gr. Finally, the reflection of dislocations resulting from the counterforces exerted by M-C_{60} and Gr contributes to the reduction in the hardness of the embedding. The spherical structure of M-C_{60} absorbs dislocations more effectively than the planar structure of graphene. This significantly reduces 1/3<100> Hirth dislocations in the embedding composites, leading to improved ductility.

3.4. Stress distribution

Fig. 8 depicts the stress distribution diagram of the five materials under different loading depths. At initial contact between the indenter and the workpiece, the stress produced by Cu and the embeddings is similar. This similarity in stress is due to the interaction between Cu and diamond at the contact surfaces of both single-crystal Cu and the embeddings. However, the contact occurs between diamond and M-C_{60} (Gr) for the coatings. The initial deformation in M-C_{60} involves compressing the spherical C_{60}, demonstrating its buffering capacity. Minor deformations in M-C_{60} do not affect stress levels in the embeddings. The deformation of high-strength Gr induces the plastic deformation of the Cu matrix, thereby leading to higher stress. As the loading depth increases, the strain range of the workpiece increases accordingly. The stress distribution is more pronounced in Cu. The stress of the coatings is predominantly localized at the interface between the indenter and the M-C_{60} (Gr). The high strength of graphene induces its plastic deformation, leading to higher localized stress at the interface. In contrast, the spherical structure of M-C_{60} evenly absorbs and reflects stress, resulting in a more uniform stress distribution across the embedding surface. The uniform stress distribution further demonstrates that M-C_{60} is better than graphene at improving the ductility of the composite in the Cu matrix.

3.5. The interaction between the M-C_{60}/Gr and the Cu

Fig. 9 shows the distribution of von Mises stress and shear strain after nanoindentation in Cu, Coatings, and Embeddings. As the loading progresses, the initial deformation occurs in the M-C_{60} at the bottom of the indenter, as seen in Fig. 9(a2). Subsequently, the spherical C_{60} gradually breaks up, forming carbon chains. Numerous carbon chains create tension, avoiding the deformation of the substrate at the bottom of the indenter. The uneven deformation of C_{60} around the indenter leads to abnormally concentrated stress in the substrate. It causes further lattice distortion (as shown in Fig. 9(b2)) and severe amorphization of nearby atoms (as shown in Fig. 10(b)). For Gr/Cu (Coating) composites, the depth increase accelerates the surface graphene's brittle fracture, as shown in Fig. 9(a4). Initial stress storage in graphene results from its high strength and shear modulus. When graphene fractures, the rapid stress release causes the atoms around the indenter to become highly amorphous, as shown in Fig. 10(d). In Cu and Embedding, stress is uniformly distributed along the direction of dislocation due to consistent dislocation movement. However, the stress on M-C_{60} and Gr at the same position is significantly lower than on Cu, as shown in Fig. 9(a1, a3, a5). It occurs because M-C_{60} and Gr absorb and reflect part of the dislocation motion while transmitting some stress to the subsequent substrate layer.

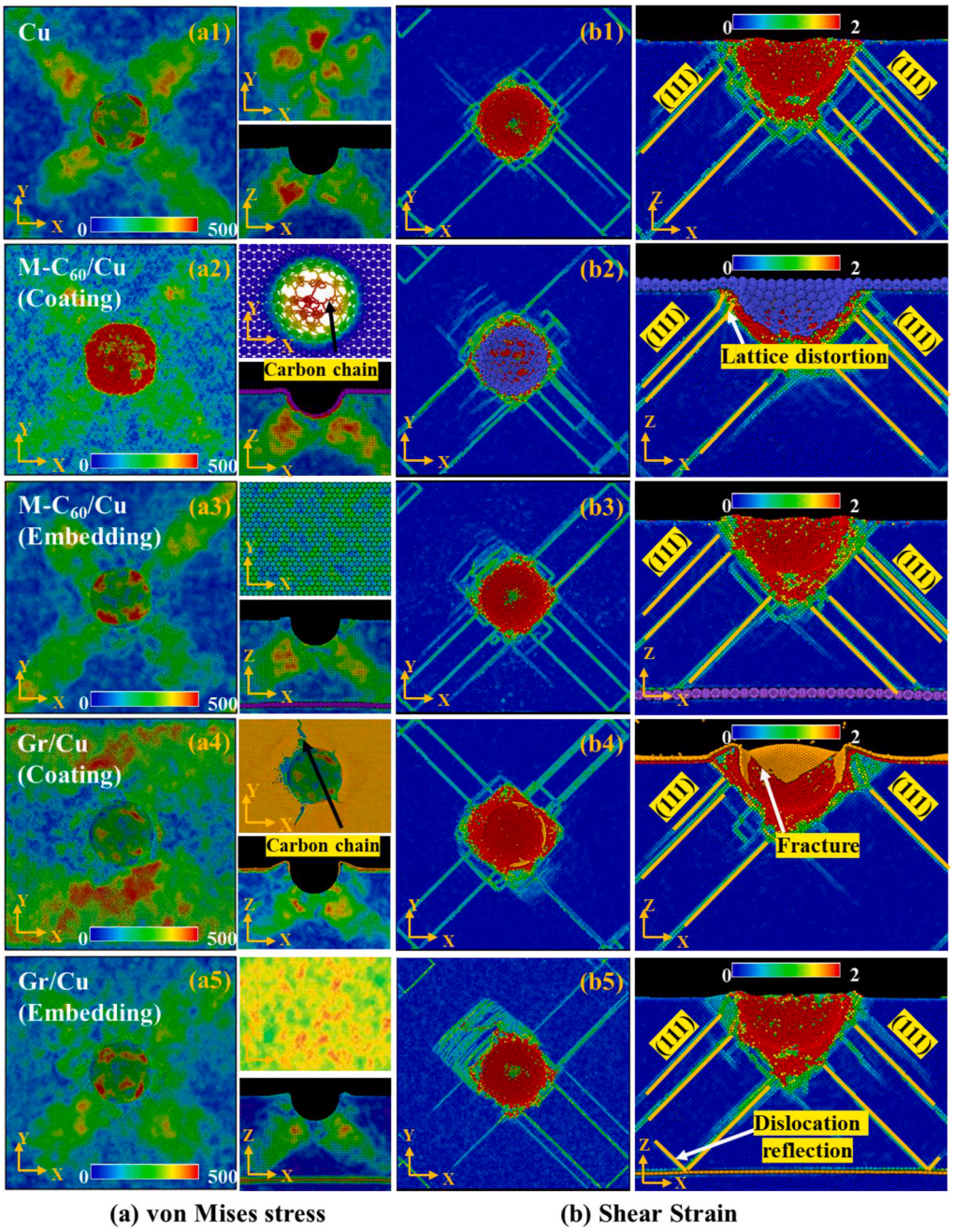

Fig. 9. The measurement for nanoindentation in xy plane and xz plane for Cu, Coatings, and Embeddings: **(a)** Von Mises stress distribution and the corresponding states of M-C_{60} and Gr, with atoms colored according to the von Mises stress values; **(b)** Shear strain distribution, with atoms colored according to the shear strain values.

This conclusion is corroborated by the shear strain diagrams and Fig. 11 (c–e). However, dislocations first reach the interface of Gr and form reflections, contributing to the higher hardness of Gr/Cu (Embedding) compared to M-C_{60}/Cu (Embedding). In addition, the stresses in all indentation tests show obvious anisotropy, leading to an anisotropic spatial distribution of the phase change structures, as shown in Figs. 9 and 10. The inherent anisotropy of M-C_{60} and Gr causes the dislocations to be anisotropic during their formation and reflection.

Nanoindentation involves various types of dislocations, including 1/2 <110> Perfect, 1/6 <112> Shockley, 1/6 <110> Stair-rod, 1/3 <100> Hirth, and 1/3 <11 > Frank dislocations [76], as illustrated in Fig. 11. The process promotes the generation of multiple shear dislocation loops. Shear dislocation loops are generated across all systems, but their sizes and numbers vary significantly. The M-C_{60} (5-11 nm) and Gr (5-6 nm) as coatings generate more and larger dislocation loops. These larger dislocation loops more effectively impede dislocation movement, thereby enhancing the strength and stiffness of the material. When M-C_{60} and Gr are embedded in the Cu matrix, partial or no dislocation loops will be generated. In addition, the M-C_{60} and Gr interface absorb dislocation lines, impeding their movement and subsequent dislocation reaction. During loading, uneven deformation of M-C_{60} in the coating induces abnormal stress on the substrate, promoting increased dislocation formation and facilitating dislocation movement and reactions. For instance, Hirth dislocations are formed by reactions between Shockley dislocations [77], such as $1/6[\bar{1}21] + 1/6[\bar{1}2\bar{1}] = 1/3[\bar{1}00]$. This process leads to the formation of larger dislocation loops.

The main difference in the mechanical properties of M-C_{60}/Cu and

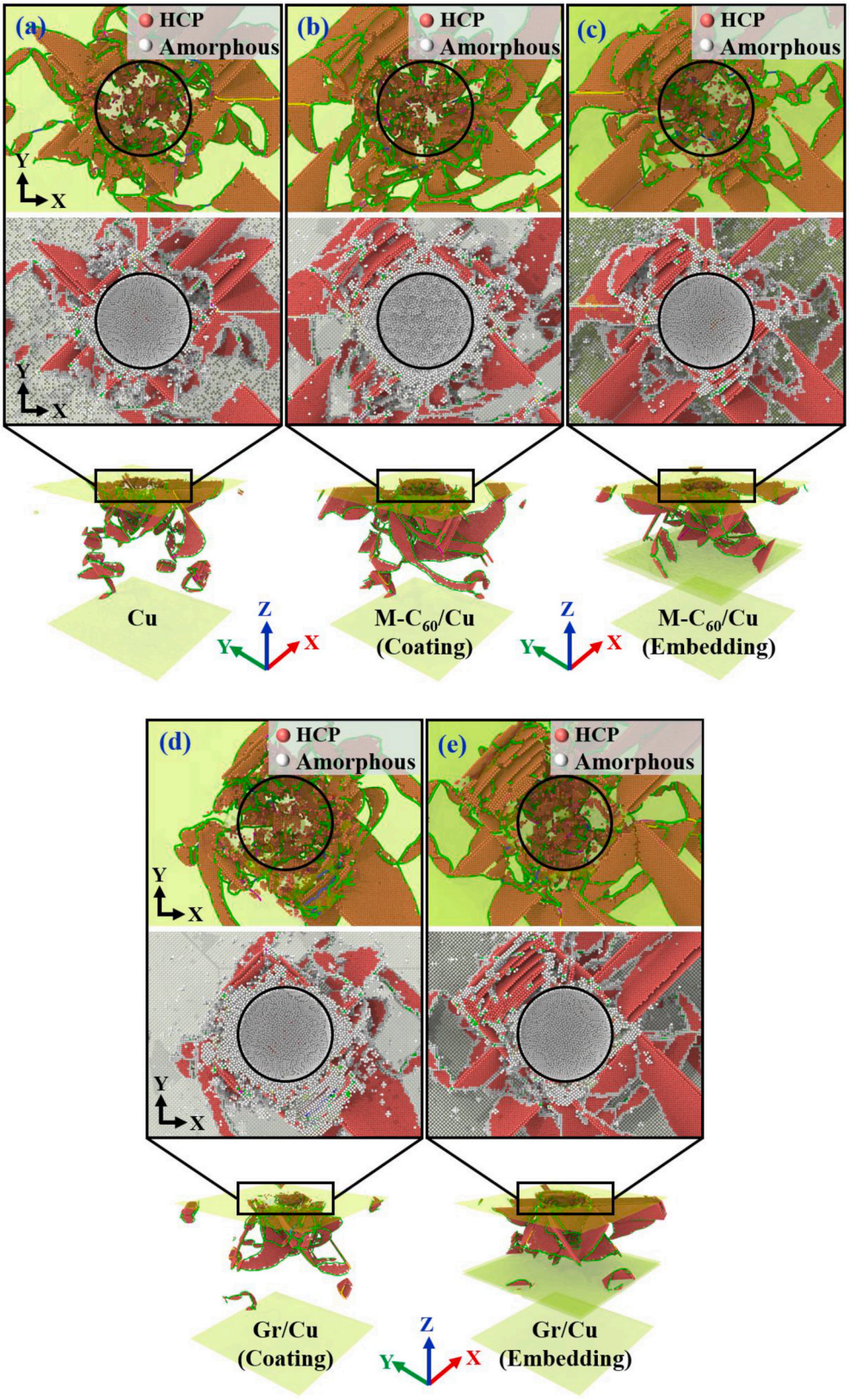

Fig. 10. Demonstration of dislocation nucleation and defect atom types after indentation for Cu, Coatings and Embeddings, where light red and white atoms represent the hcp structure and amorphous structure, respectively. (For interpretation of the references to color in this figure legend, the reader is referred to the Web version of this article.)

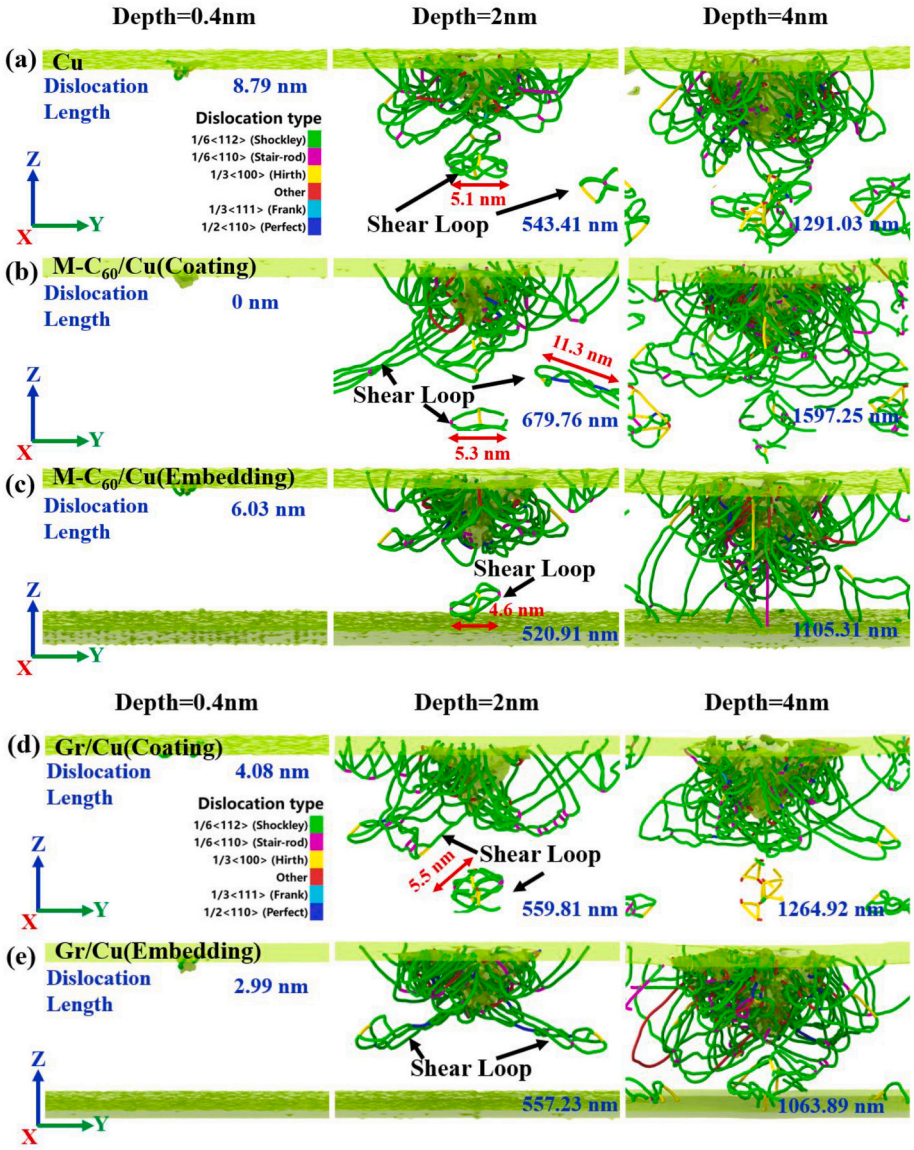

Fig. 11. Evolution of dislocation nucleation and movement in the yz plane at the 0.4 nm, 2 nm, and 4 nm depths for Cu, Coatings, and Embeddings, with lines of different colors representing different dislocations. (For interpretation of the references to color in this figure legend, the reader is referred to the Web version of this article.)

Gr/Cu composites lies in the structural differences between M-C_{60} and Gr. Coordination number(CN) of M-C_{60} and Gr in composites at an indentation depth of 4 nm, as shown in Fig. 12. The primary peak of graphene appears at CN ≈ 3, while that of monolayer fullerene is distributed between CN ≈ 3~4, with a broader range. Additionally, for CN > 4, the proportion of monolayer fullerene is significantly higher than that of graphene (which is 0 in Gr/Cu(Embedding)). This indicates that during the indentation process, graphene maintains a high degree of layered structural integrity, without significant local collapse or phase transformation. In contrast, due to spherical curvature effects, monolayer fullerene undergoes local deformation, forming a denser structure. This deformation may lead to partial atomic rearrangement, enhancing local short-range order and increasing coordination number. This also suggests that the sp^2-sp^3 hybrid structure of M-C_{60} provides multiple bonding sites (48 per nm^2), enhancing adhesion with the copper matrix. Meanwhile, the spherical fullerene cages of M-C_{60} provide mechanical interlocking, further strengthening the interface. Graphene, with its purely sp^2 structure, has 26.3% fewer bonding sites (38 per nm^2) than M-C_{60}. This results in lower adhesion energy and interfacial strength. However, the planar structure of graphene allows for a larger contact

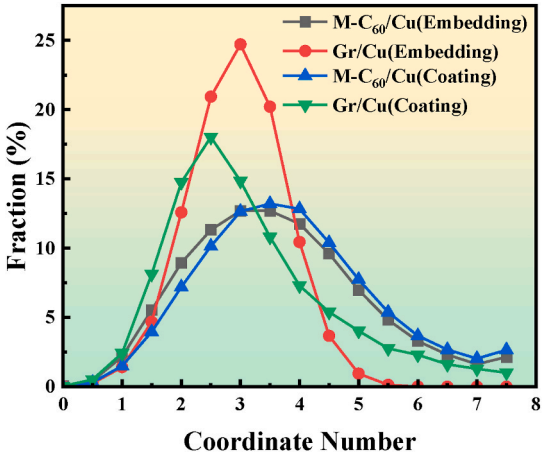

Fig. 12. Coordination number of M-C_{60} and Gr in M-C_{60}/Cu and Gr/Cu composites at an indentation depth of 4 nm.

area, partially compensating for the lower bonding strength.

3.6. Characteristics under different conditions

3.6.1. Loading speed effect

As illustrated in Fig. 13(a1-e1), the force-displacement curves of five materials are presented under varying loading speeds (V). For each material, the load increases elastically with depth, reaches a peak associated with the elastic-plastic transition. Drop was observed during the pop-in event, and subsequently exhibited a gradual rise in occurrence with further loading. Although the absolute indentation speeds in MD simulation are high, we classify the tests into two regimes: low strain

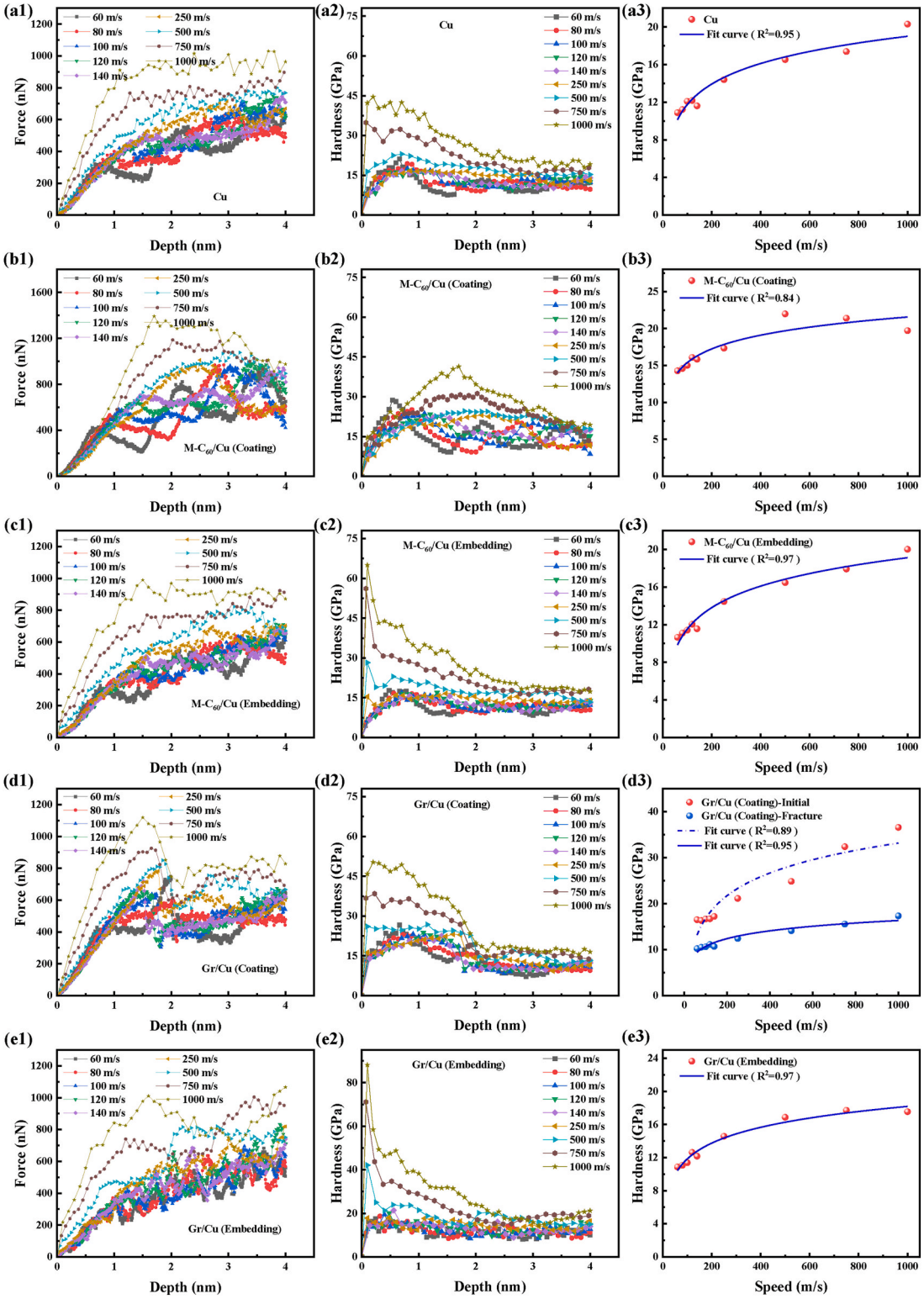

Fig. 13. Variation of **(a1-e1)** Force, **(a2-e2)** Hardness and **(a3-e3)** Average hardness (Non-ISE area) of different materials with indentation depth at different loading speeds. The blue curve is the fitting curve of the average hardness. (For interpretation of the references to color in this figure legend, the reader is referred to the Web version of this article.)

rate (V < 140 m/s) and high strain rate (V > 140 m/s). At low strain rates, the force in the elastic regime varies little with speeds for Cu and the embedded composites, **see Appendix (Fig. A2)**. At high strain rates, the curves shift upward with increasing speeds, resulting in elevated peak values and load at a given depth. Interestingly, for the coating composites the load at a fixed depth first decreases with increasing speed in the low-rate regime and then increases at higher speeds. This indicates a rate-dependent mechanism that governs the strength–ductility balance in 2D/metal composites. In M-C_{60}/Cu (Coating), higher speed accelerates the deformation of the spherical C_{60} units and promotes carbon-chain formation. This, in turn, intensifies chain rupture, though complete failure does not occur, as shown in Fig. 14(a). In Gr/Cu (Coating), the surface graphene undergoes complete brittle fracture at all speeds, with the onset shifting to shallower depths as speeds increase, as shown in Fig. 14(b).

The depth dependence of hardness at different velocities is shown in Fig. 13(a2-e2). All five materials exhibit a pronounced indentation size effect (ISE), characterised by an initial increase in hardness at shallow depths, followed by a decline towards a plateau. Similarly, the average hardness of the No-ISE area was calculated. However, for Gr/Cu (Coating), prior to the fracture of the graphene, the maximum hardness is taken as the representative value. This is due to the fact that an increase in speed results in earlier fracture and a substantial reduction in the No-ISE window, thereby rendering the average unreliable. For each material, the average hardness increases with speed and then approaches saturation. This behavior can be explained using thermally activated slip model of Kocks–Argon–Ashby [78], with the strain rate dependence given by Eq. (16).

$$\dot{\varepsilon} = \dot{\varepsilon}_0 \exp\left[-\frac{\Delta G(\tau)}{kT}\right] \tag{16}$$

where, $\Delta G(\tau)$ is the activation free energy of the rate-controlling process under the applied shear stress τ. It represents the thermal energy barrier that must be overcome for plastic flow—such as dislocation nucleation/slip or interfacial shear—to occur at the specified stress. $\dot{\varepsilon}$ denotes the mechanism-specific plastic strain rate (s^{-1}). In nanoindentation, it is typically taken as the indentation strain rate. $\dot{\varepsilon}_0$ is reference strain rate (s^{-1}), typically treated as a constant. k is the Boltzmann constant, and T is the absolute temperature (K).

Hirth [79] combined the Gibbs free-energy barrier with a mechanical work term and introduced the activation volume, yielding

$$\Delta G(\tau) = \Delta G_0 - V^* \tau \tag{17}$$

Here, ΔG_0 is the activation barrier in the absence of mechanical loading, and V^* is the activation volume.

In addition, the flow stress beneath the indenter tip is proportional to the measured hardness during nanoindentation, can be expressed as [80].

$$H \approx C\tau \tag{18}$$

From Eqs. (16)–(18), we obtain

$$H(\dot{\varepsilon}) = H_0 + \frac{kT}{V^*}\ln\left(\frac{\dot{\varepsilon}}{\dot{\varepsilon}_0}\right) \tag{19}$$

Equation (19) shows that, with constant temperature, the hardness initially increases and then levels off as the strain rate increases, as shown in Fig. 13 (a3-e3). This is consistent with our results. An exception is the M-C_{60}/Cu (Coating) configuration, which shows a decrease in hardness with increasing strain rate. This deviation highlights the limited applicability of Eq. (19) to 2D surface coatings: the relation assumes an intact, stable rate-controlling mechanism, whereas in our tests the surface layer fractures (graphene fails by complete brittle fracture, and M-C_{60} evolves from localized to widespread rupture), invalidating the activation-volume description.

Fig. 15(a1-e1) presents the dislocation density-displacement curves for the five materials at different loading speeds. For all cases, the dislocation density increases with indentation depth. At low strain rates, the change in dislocation density of each material does not demonstrate a clear pattern with increasing loading speed. At high strain rates, however, increasing speed shifts the curves downward: at the same displacement, higher rates yield lower dislocation densities. This behavior contradicts the expectation from Taylor Forest hardening [81], where the flow stress on an active slip system scale with the square root of dislocation density:

$$\tau = \alpha G b\sqrt{\rho_m} \tag{20}$$

where α is a dimensionless constant (typically 0.2-0.5), G is the shear modulus, b is the magnitude of the Burgers vector, and ρ_m is the dislocation density.

As demonstrated in Eq. (18), a direct correlation can be established

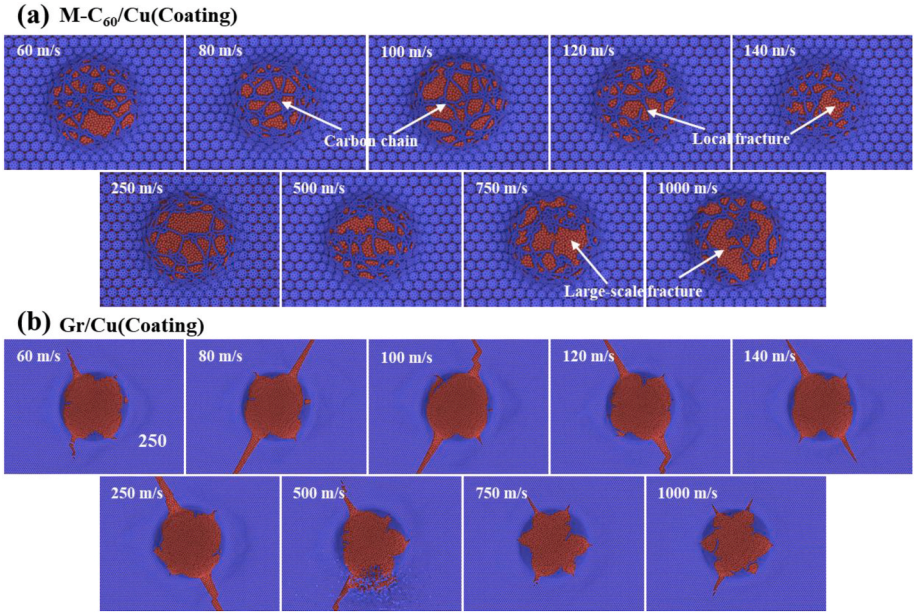

Fig. 14. Deformation and fracture of **(a)** M-C_{60}/Cu(Coating) and **(b)** Gr/Cu(Coating) at different loading speeds.

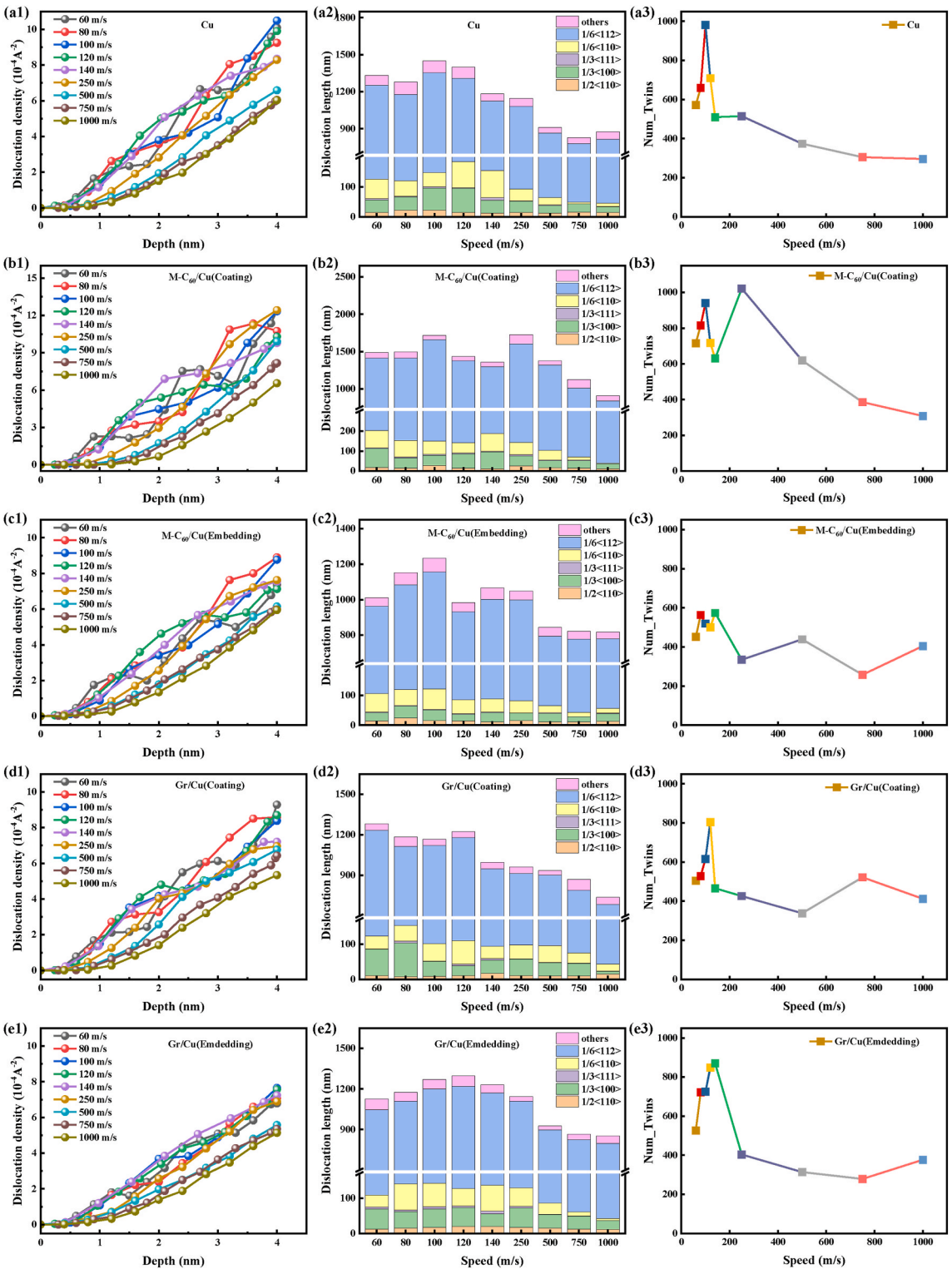

Fig. 15. At different loading speeds, **(a1-e1)** Variation of dislocation density with indentation depth; **(a2-e2)** Lengths of different types of dislocations inside the substrate; **(a3-e3)** The number of twin boundary atoms produced.

between hardness and dislocation density:

$$H = CM\alpha Gb\sqrt{\rho_m} \tag{21}$$

where M is the Taylor factor that converts the resolved shear stress τ into the equivalent uniaxial (tensile) flow stress.

It is evident from the derived relation that hardness increases in proportion to dislocation density. Notably, however, our earlier results show that hardness rises with loading velocity while the dislocation density decreases. This implies that Taylor forest hardening does not govern the response at high strain rates, and the hardness–dislocation density relationship under these conditions warrants further study. Tang [82] et al. reported that, at extreme strain rates, dislocation motion transitions from thermally activated glide to ballistic transport due to strong dislocation–phonon interactions, which introduce substantial

drag and can even lead to dislocation annihilation. The relationship between the dislocation glide velocity (v) and the analytical shear stress (τ), as determined by the drag effect of phonons [83], is as follows:

$$v = \frac{b\tau}{\dot{B}} \tag{22}$$

where, $\dot{B}$ is the viscous drag coefficient governing dislocation motion.

According to the Orowan relation [84], the plastic shear strain rate is

$$\dot{\varepsilon} = \rho_m b v \tag{23}$$

By eliminating the common term (dislocation velocity), we obtain

$$\tau = \frac{\dot{B}\dot{\gamma}}{b^2\rho_m} \tag{24}$$

For macroscopic measurements, applying the Taylor/Schmid conversions $\sigma = M\tau$ and $\dot{\varepsilon} = \dot{\gamma}/M$ gives

$$\sigma = \frac{M\dot{B}\dot{\varepsilon}}{b^2\rho_m} \Rightarrow H = \frac{CM\dot{B}\dot{\varepsilon}}{b^2\rho_m} \tag{25}$$

Consequently, the plastic strain rate is inversely proportional to the mobile dislocation density, consistent with our findings.

To elucidate the hardening mechanisms at low strain rates, we compared the evolution of dislocation lengths for different character types, as shown in Fig. 15(a2-e2). Shockley partial dislocations dominate, followed by Stair-rod and Hirth dislocations. Perfect and Frank dislocations are relatively rare. With increasing loading speed, the total dislocation length in the embedded composites and in Cu grows markedly, consistent with forest hardening. The coating systems do not follow this trend, likely due to be fractured of the surface layer. This hypothesis requires further verification. Notably, in the coatings, the total lengths of stair-rod and Hirth dislocations increase, promoting the nucleation of dislocation loops, Lomer–Cottrell locks, and Hirth locks, as shown in Fig. 16(b–d), which impede plastic flow and raise hardness.

Twinning provides a distinct carrier of plasticity beyond dislocation slip, and observing twin formation reveals the strain hardening of crystals. Twin boundaries act as strong barriers to slip (similar to a Hall–Petch effect). We identified twin-boundary atoms using PTM in OVITO followed by planar-defect analysis. The number of twinned atoms with loading speed is shown in Fig. 15(a3–e3). The results show that at low strain rates, the number of twin atoms increases with

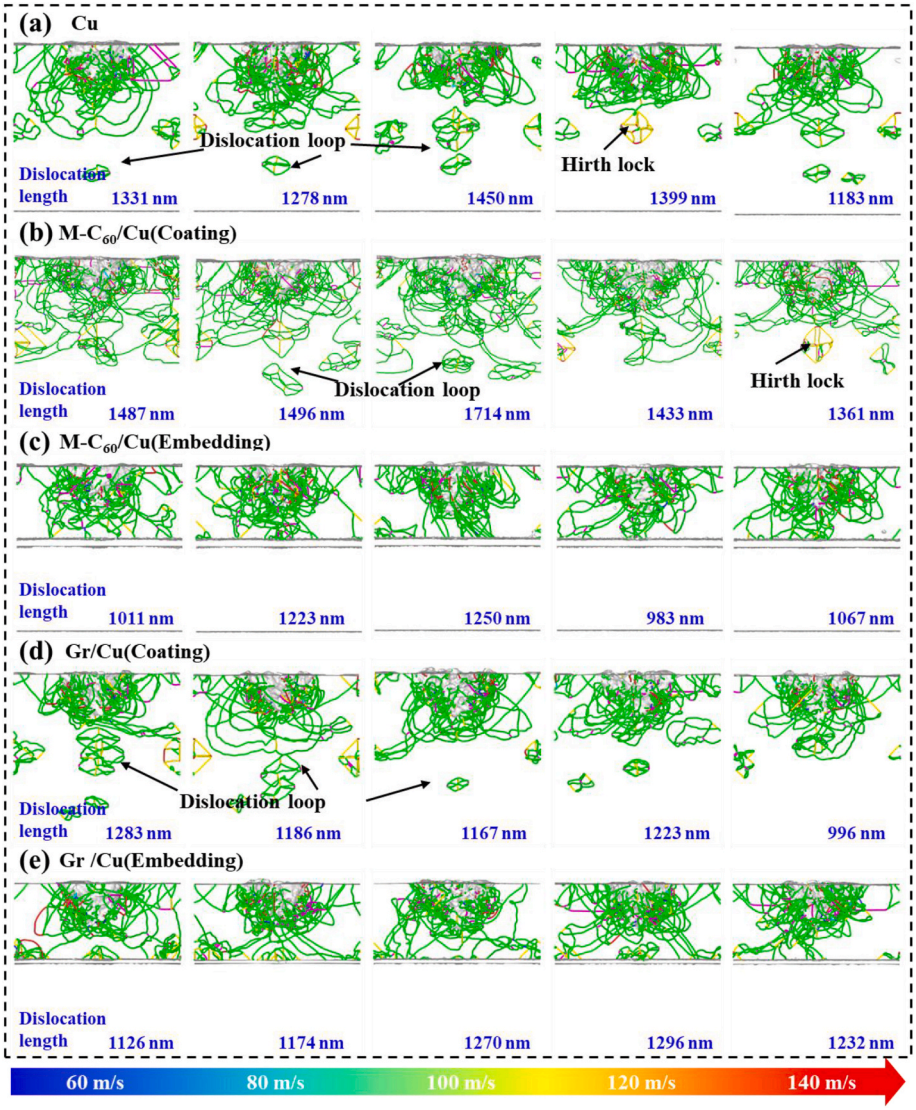

Fig. 16. DXA analysis of **(a)** Cu; **(b)** M-C_{60}/Cu(Coating); **(c)** M-C_{60}/Cu(Embedding); **(d)** Gr/Cu(Coating); **(e)** Gr/Cu(Embedding) at different loading speeds, with lines of different colors representing different dislocations. (For interpretation of the references to color in this figure legend, the reader is referred to the Web version of this article.)

increasing speed, while the opposite trend occurs at high strain rates (the trend is not strictly monotonic, but the overall tendency is plausible). In the coating systems, the M-C_{60} coating generates substantially more twinned atoms than the graphene layer. This is attributed to stronger Cu-C bonding and the uneven surface of the M-C_{60} coating (see section 3.5). By contrast, graphene possessed very high in-plane stiffness effectively suppresses stacking faults and partial twinning.

Our results corroborate previous conclusions on rate hardening in metals. However, the discrepancy observed between hardness and dislocation density at high strain rates challenges the conventional

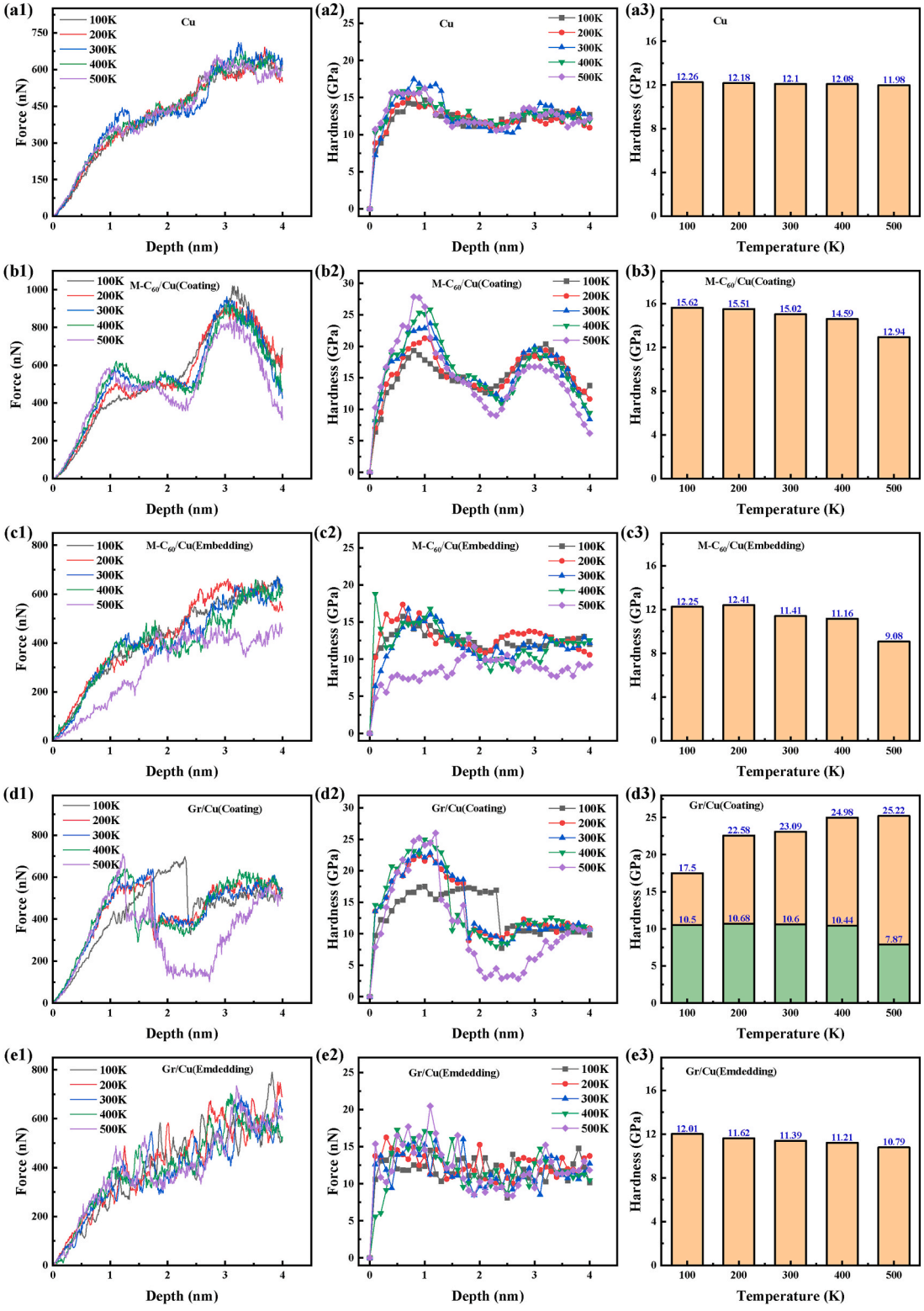

Fig. 17. Variation of **(a1-e1)** force, **(a2-e2)** hardness and **(a3-e3)** average hardness (Non-ISE area) of different materials with indentation depth at different temperatures. The blue curve is the fitting curve of the average hardness. (For interpretation of the references to color in this figure legend, the reader is referred to the Web version of this article.)

forest hardening model and instead aligns with a phonon-drag-controlled mobility mechanism. Regarding twinning behavior, the promotion of twinning by the M-C_{60} coating extends prior knowledge by revealing how molecular-scale roughness and bonding heterogeneity can locally amplify shear stress. In summary, dislocation forest hardening dominates at low strain rates, whereas pronounced strain-rate hardening emerges at high strain rates, consistent with literature [85].

$$H = \begin{cases} CM\alpha Gb\sqrt{\rho_m}, Low\ strain\ rate \\ \dfrac{CMB\dot{\varepsilon}}{b^2\rho_m}, High\ strain\ rate \end{cases} \tag{26}$$

3.6.2. Temperature effect

Fig. 17(a1-e1) shows the force-displacement curves of the five

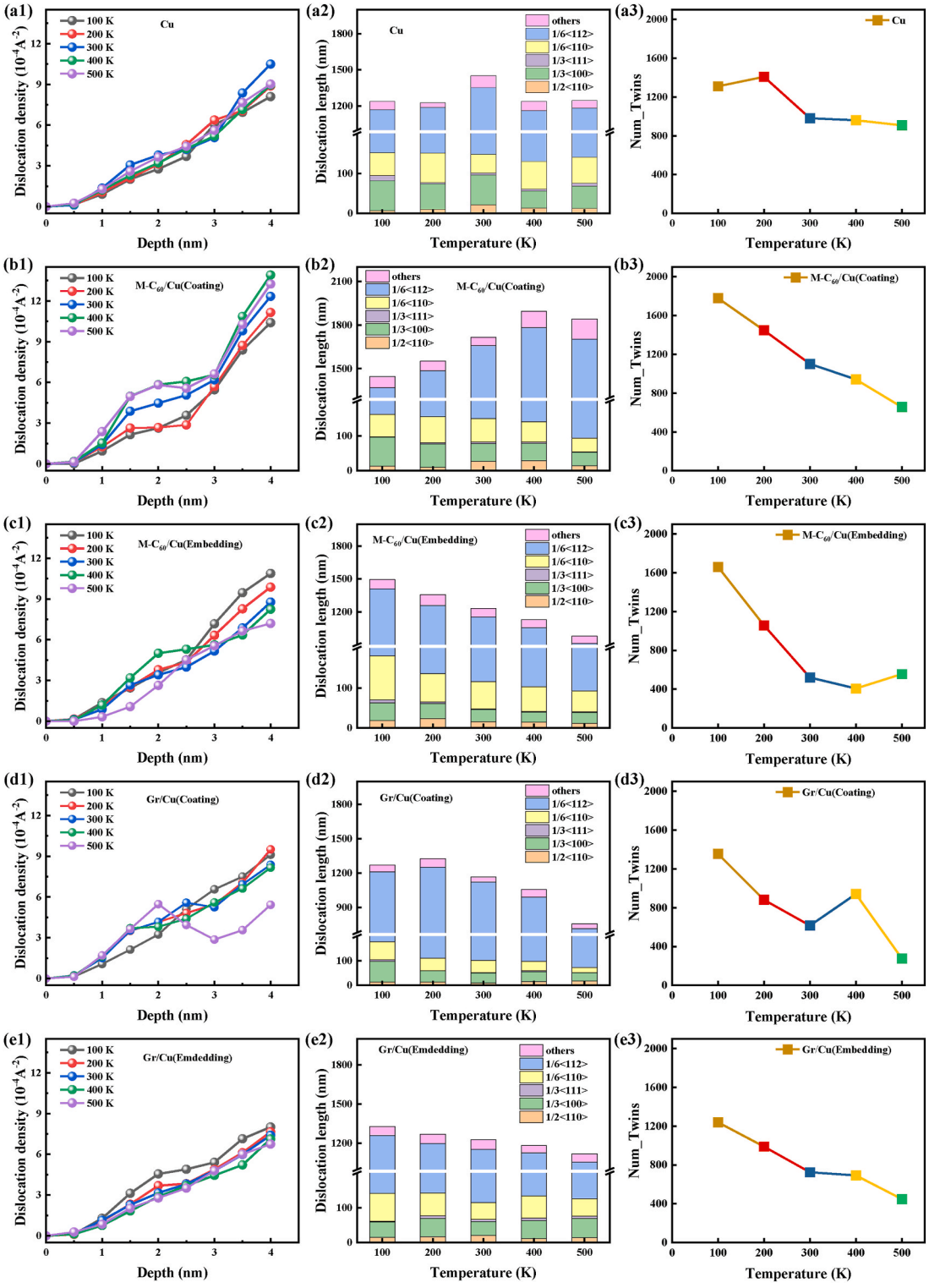

Fig. 18. At different temperatures, **(a1-e1)** Variation of dislocation density with indentation depth; **(a2-e2)** Lengths of different types of dislocations inside the substrate; **(a3-e3)**The number of twin boundary atoms produced.

materials at different temperatures (T). For each material, the load increases with depth. The Cu curves nearly overlap across temperatures, indicating weak thermal sensitivity. For the M-C_{60}/Cu composites, the curves shift downward with increasing temperature. In the embedded configuration, this decrease is most pronounced at T = 500 K. For Gr/Cu (coating), prior to graphene fracture, the load is the highest among all systems and shifts upward with temperature, but elevated temperature promotes earlier fracture of the graphene. After fracture, the response resembles that of Cu—overall weak temperature dependence—with a dip at T = 500 K followed by recovery to a comparable level. Gr/Cu (Embedding) behaves similarly to M-C_{60}/Cu (Embedding), with loads decreasing as temperature increases, although the change trend is not obvious.

The hardness–depth curves at different temperatures is shown in Fig. 17(a2-e2), and mirror the features of the corresponding force–displacement responses. The variation of the average hardness with temperature in the stable stage is shown in Fig. 17(a3-e3). For each material, the average hardness generally decreases with temperature. However, Cu and Gr/Cu (Coating)-fracture exhibit weak temperature sensitivity, consistent with literature [86]. The combined dependence of hardness on temperature and strain rate can be captured by a Johnson–Cook–type expression [87]:

$$H(T) = H_0\left[1 + A\ln\left(\frac{\dot{\varepsilon}}{\dot{\varepsilon}_0}\right)\right][1 - mT^*], T^* = \frac{T - T_{\text{room}}}{T_{\text{melt}} - T_{\text{room}}} \quad (27)$$

Here, A is the strain-rate sensitivity coefficient (dimensionless), and m is the thermal-softening exponent (dimensionless). T, T_{room}, and T_{melt} are the test temperature, room temperature, and melting temperature, respectively.

The overall hardness ranking is Gr/Cu (Coating)-initial > M-C_{60}/Cu (Coating) > Cu > M-C_{60}/Cu (Embedding) ≈ Gr/Cu (Embedding) > Gr/Cu (Coating)-fracture, consistent with our earlier results.

Fig. 18(a1-e1) shows how dislocation density varies with temperature. For all five materials, the dislocation density increases steadily with indentation depth. As temperature rises, the Cu curves cluster tightly. In the 2D/metal composites, dislocation density generally decreases with increasing temperature—except for M-C_{60}/Cu (Coating), where it increases with temperature. This trend appears inconsistent with the concurrent decrease in hardness at higher temperatures and therefore merits further investigation. Fig. 18(a2-e2) decomposes the dislocation type by character. During plastic deformation, Shockley partials dominate slip and diminish with increasing temperature, with

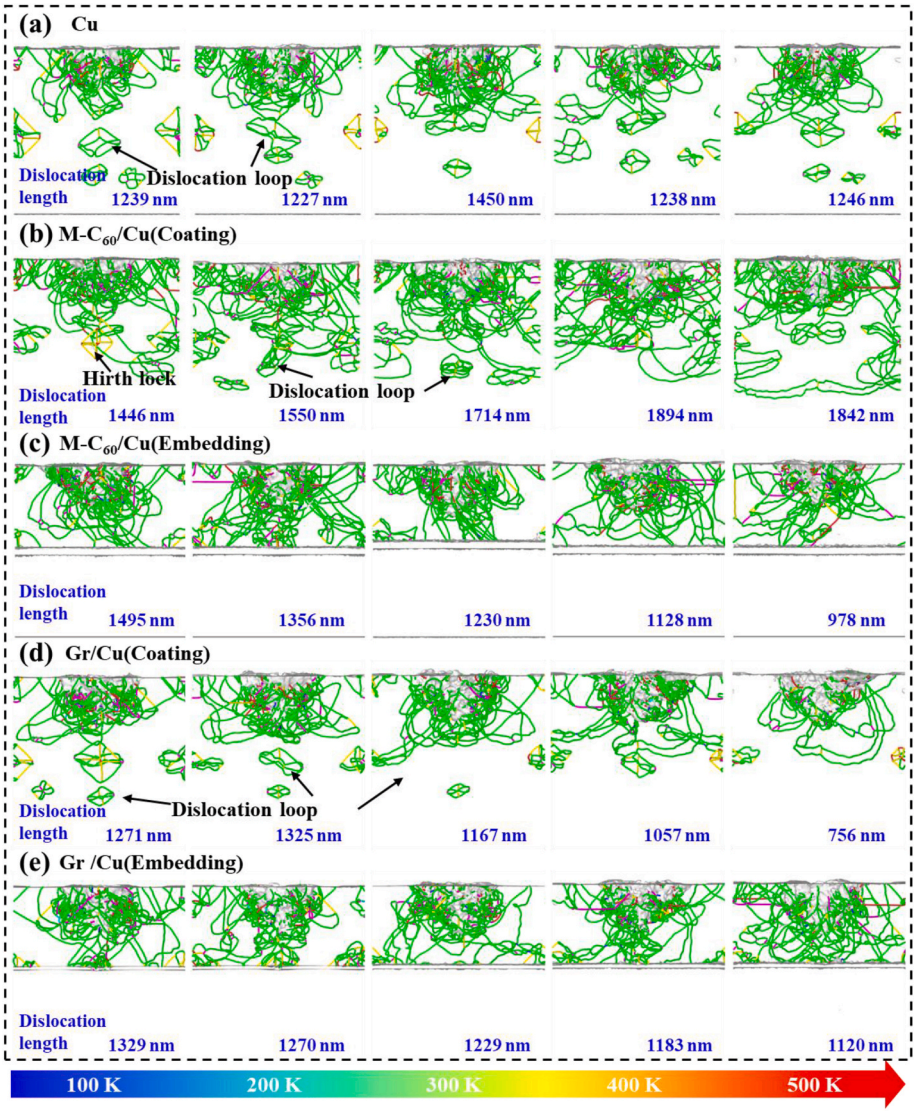

Fig. 19. DXA analysis of **(a)** Cu; **(b)** M-C_{60}/Cu(Coating); **(c)** M-C_{60}/Cu(Embedding); **(d)** Gr/Cu(Coating); **(e)** Gr/Cu(Embedding) at different temperatures, with lines of different colors representing different dislocations. (For interpretation of the references to color in this figure legend, the reader is referred to the Web version of this article.)

the exceptions of Cu and M-C_{60}/Cu (Coating). In Cu, Shockley partial dislocations remain nearly constant. For M-C_{60}/Cu (Coating), they increase with increasing temperature, consistent with the change in dislocation density. Sessile products—stair-rod, Hirth, and Frank dislocations—generally decline with temperature, while in Cu their populations remain nearly constant. Perfect dislocations approach saturation overall.

From the twin analysis of Fig. 18(a3-e3), it can be seen that the number of twinned atoms decreases with temperature in all systems: Cu shows a slight reduction; M-C_{60}/Cu (Embedding) exhibits the largest drop, though twinning is suppressed again at the highest temperatures. At low temperature, M-C_{60}/Cu (Coating) retains a comparatively high density of twins, consistent with the propensity for mechanical twinning on (111) by Shockley partials under low-temperature or high-rate conditions [88]. Consequently, even though the total dislocation density in M-C_{60}/Cu (Coating) can be low at low temperature, the abundance of twin boundaries together with dislocation loops and Hirth/Lomer–Cottrell locks impede slip and increases the crystal strength.

Overall, increasing temperature enhances dislocation mobility—via cross-slip and climb—and promotes annihilation, thereby lowering the dislocation density and suppressing twinning, as shown in Fig. 19(c–e). It also reduces the formation of dislocation loops and sessile locks (Lomer–Cottrell and Hirth locks), as shown in Fig. 19(a, b, d). The exceptions—the anomalous increase in dislocation density in M-C_{60}/Cu coatings—underscore the distinct interfacial mechanics of surface-modified metals. For M-C_{60}/Cu, strong Cu–C bonds and rough coating morphology may promote Shockley partial dislocation nucleation even at high temperatures.

3.6.3. Berkovich nanoindentation

To investigate the generality of the observed reinforcement mechanisms and hardness trends, we performed additional nanoindentation simulations using a Berkovich indenter. This allows assessment of whether indenter geometry influences the composite's mechanical response and ensures that our findings are not artefacts of using a spherical indenter. The model configuration and parameter settings are provided in Appendix 2.

3.6.3.1. Force-displacement relationship. Fig. 20(a) shows the force-depth curves for Cu and 2D/Cu composites under nanoindentation with a Berkovich indenter. All five materials exhibit a pronounced nonlinear increase in load with depth. The serrated nature of the curves is characteristic of discrete dislocation nucleation and expansion events beneath the indenter tip. At the same indentation depth, the coating systems can sustain significantly higher loads than pure Cu. Among them, the graphene coating sustains the highest load in the early stage, consistent with graphene's exceptionally high in-plane stiffness and its load-transfer capability across the contact interface. As the graphene fractures, a sudden dropping appears in the curve. Notably, the abrupt load drop caused by the Berkovich indenter is less pronounced than that produced by a spherical indenter, owing to the difference in their contact areas with the substrate, as shown in Fig. 21(b).

As indentation proceeds, although graphene fractures in both cases, with the Berkovich indenter most of the conical surface still contacts the 2D interface, and only a small portion of the tip directly interacts with the Cu substrate. The deformation of the substrate thus results from the combined effects of load transfer through the 2D contact surface and direct tip–substrate contact. For the spherical indenter, the tip eventually makes full direct contact with the Cu, and the subsequent load–displacement curve approaches that of pure Cu, as shown in Section 3.1. Graphene fracture also enables the M-C_{60} coating system to exhibit the highest load capacity. Throughout the indentation process, $M-C_{60}$ does not undergo the deformation and fracture observed under spherical indentation. Instead, it only engages in load transfer through the 2D interface, as shown in Fig. 21(a). Since the M-C_{60} layer is a 2D interface composed of interconnected spherical C_{60} molecules, the load-transfer process is equivalent to multiple spherical C_{60} particles acting on the Cu substrate, causing uneven deformation and promoting a surge

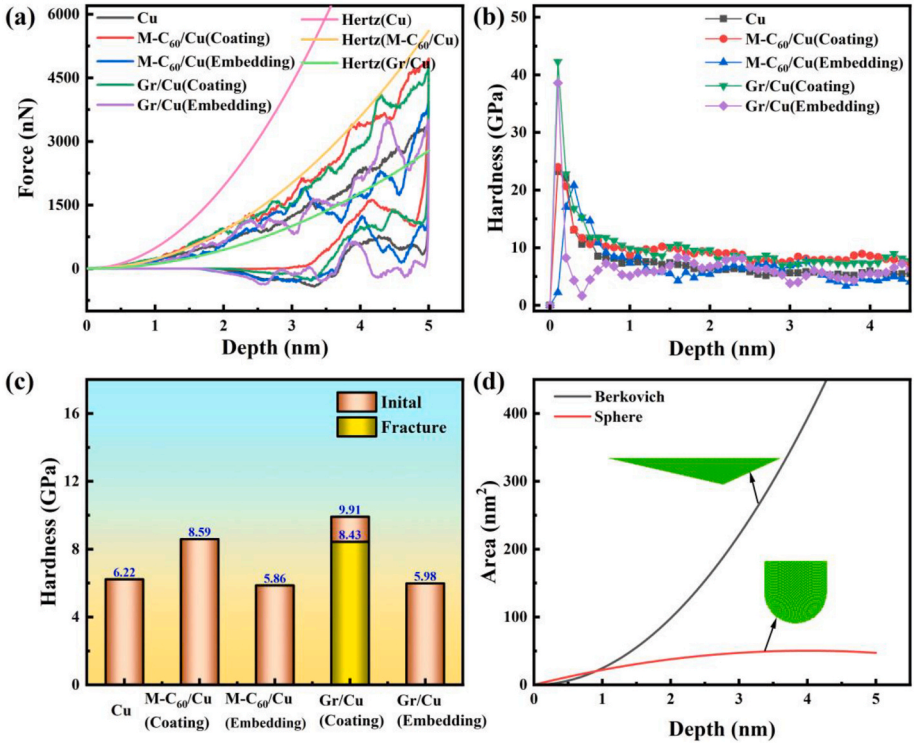

Fig. 20. Evolution of force **(a)** and hardness **(b)** with indentation depth for different materials by Berkovich indenter; **(c)** Average hardness of non-ISE area for five materials, with yellow representing the hardness of Gr/Cu (Coating) after graphene breaks; **(d)** Variation of contact area between different indenter geometries and the workpiece during loading. (For interpretation of the references to color in this figure legend, the reader is referred to the Web version of this article.)

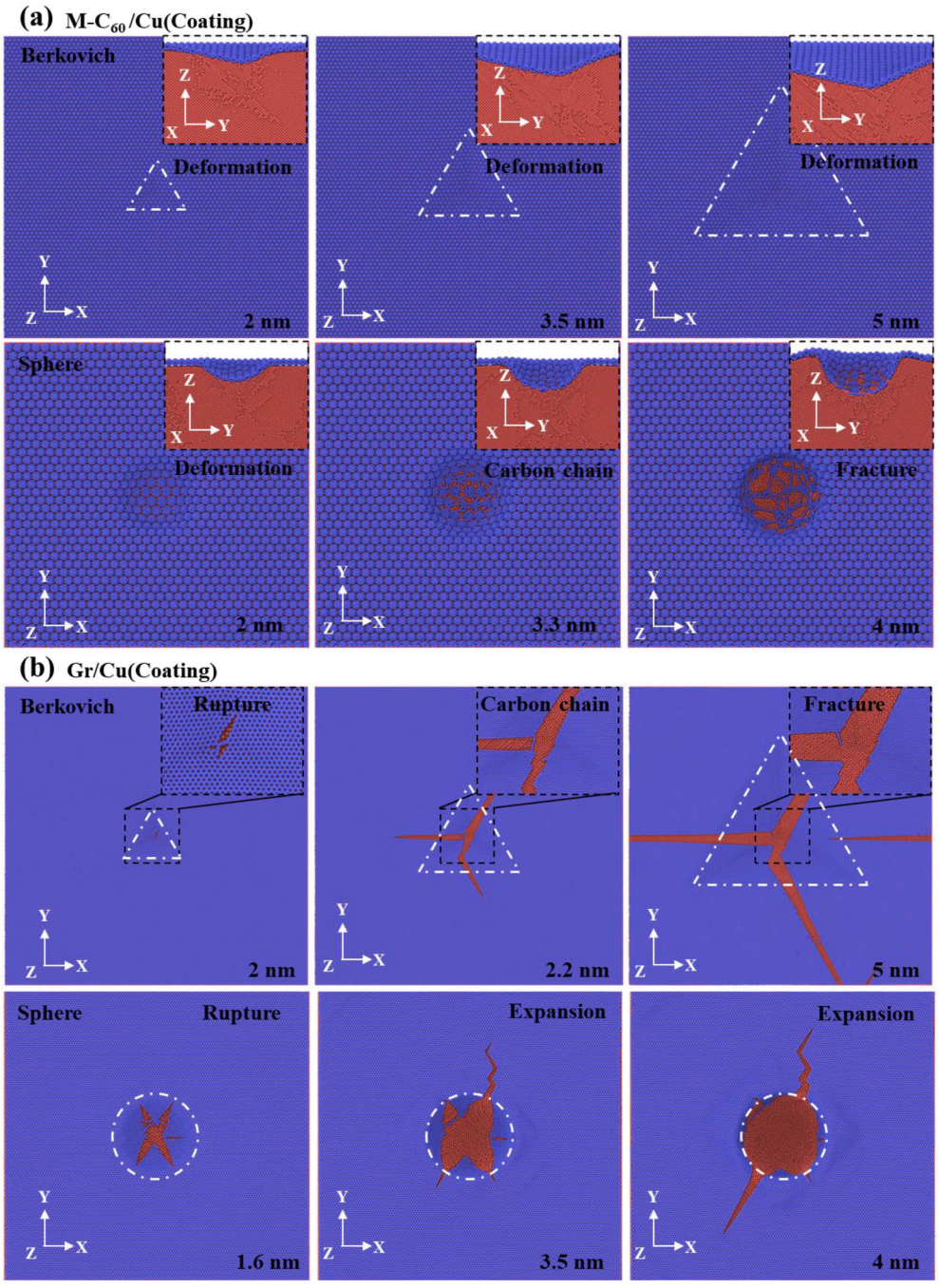

Fig. 21. Deformation and fracture of **(a)** M-C_{60}/Cu(Coating) and **(b)** Gr/Cu(Coating) under different indenter geometries.

in geometrically necessary dislocations (GNDs).

The embedding systems, regardless of indenter geometry, display softened plastic deformation due to the blocking and constraining effects of the internal 2D interface on dislocation slip. Fig. 20(b, c) compare hardness-depth curves and average hardness values. All curves reach a peak at shallow depths and then decay to a steady state (non-ISE region). This peak results from the ISE caused by the sharp Berkovich tip, which triggers a burst of GNDs. As indentation depth increases, the GND density per unit contact area saturates, and hardness stabilizes. The ranking of average hardness values matches the results obtained with the spherical indenter, with the hardness of Cu close to that reported in Ref. [89]. However, the values are lower than those for the spherical indenter, due to differences in contact area, as shown in Fig. 20(d). At shallow depths, the spherical indenter's contact area (A_S) is larger than that of the Berkovich indenter (A_B) at the same depth, resulting in a lower mean contact pressure (hardness) and a smoother onset of plasticity. As depth increases, A_B grows faster and eventually exceeds A_S; the sharper tip then engages more material, leading to relatively lower hardness values. It is noteworthy that, after graphene fracture, the hardness of the Gr coating system remains higher than that of Cu (unlike the spherical indenter case), benefiting from residual Gr fragments and interfacial friction.

3.6.3.2. Dislocation evolution. Fig. 22 presents the dislocation density of the five materials at various indentation depths. At shallow depths, the dislocation density remains constant in an elastic regime, followed by a sharp jump at the first pop-in event. As new dislocation sources are activated and existing dislocations expand, the dislocation density

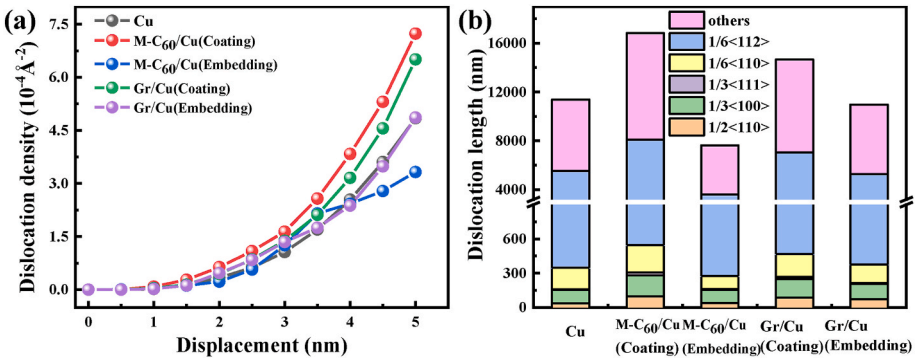

Fig. 22. (a) Variation of dislocation density with indentation depth; **(b)** Lengths of different types of dislocations inside the substrate.

increases monotonically with depth. In the coating systems, the onset of initial dislocation bursts is delayed, as the M-C_{60} and Gr increase the nucleation barrier and their in-plane stiffness shields the near-surface shear field. Once this barrier is overcome, local dislocation multiplication becomes active. In the embedding systems, the nucleation of initial dislocations is similar to that in Cu, as the surface remains Cu. However, when the plastic zone encounters the embedded 2D interface, it promotes dislocation annihilation and reflection.

The length comparison of different dislocation types generated in various matrices is shown in Fig. 22(b). Apart from amorphous atoms, Shockley dislocations are the main carriers of slip and key components of deformation twins. Perfect dislocations are usually short because they quickly dissociate into two Shockley partial dislocations separated by a stacking fault. Immobile dislocations (stair-rod, Hirth, and Frank) tend

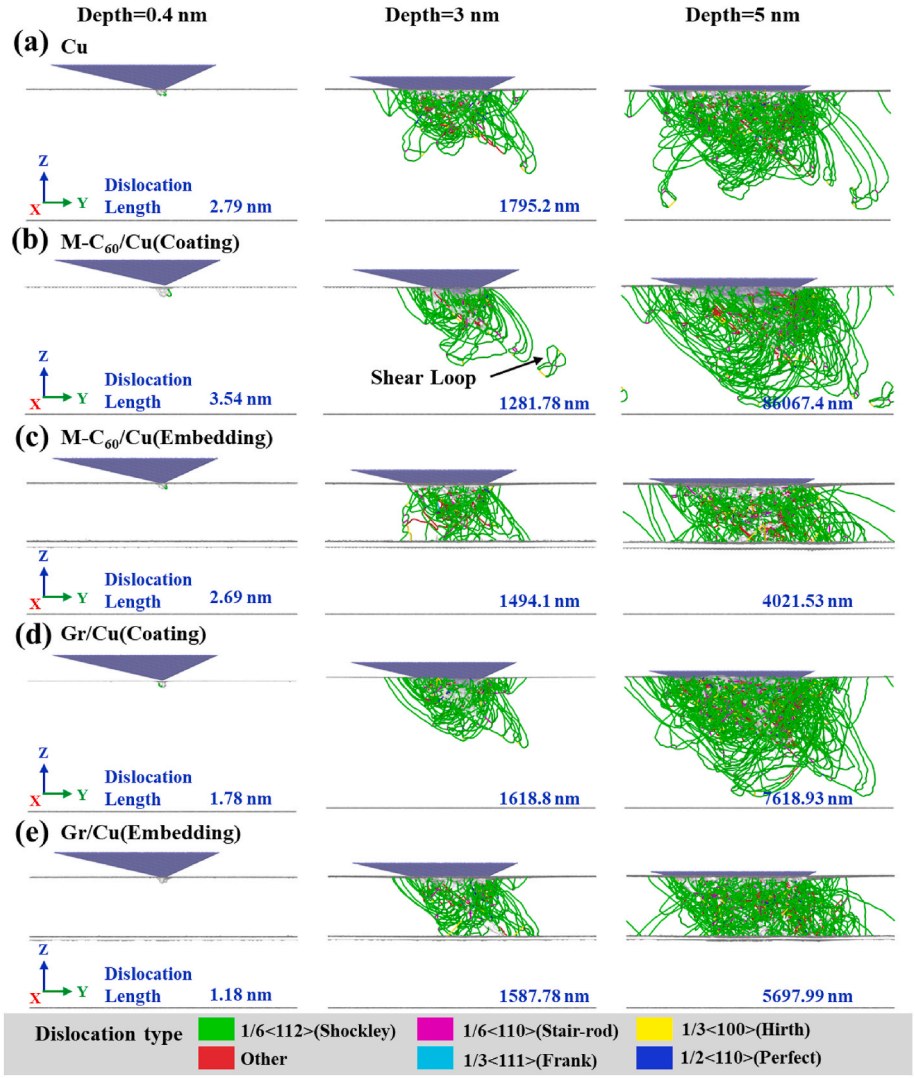

Fig. 23. Evolution of dislocation nucleation and movement in the yz plane at the 0.4 nm, 3 nm, and 5 nm depths for Cu, Coatings, and Embeddings, with lines of different colors representing different dislocations. (For interpretation of the references to color in this figure legend, the reader is referred to the Web version of this article.)

to form immobile locks that hinder dislocation motion, thereby enhancing work hardening. The coating interfaces promote higher proportions of stair-rod and Hirth dislocations through cross-slip and reactions, locking mobile dislocation lines and strengthening the material. The M-C_{60} coating is more prone to producing dislocation loops than the Gr coating due to the uneven deformation of interfacial Cu, as shown in Fig. 23(b), which further impedes dislocation multiplication and propagation. This explains why M-C_{60}/Cu (Coating) exhibits higher hardness than Gr/Cu (Coating). In the embedding systems, the 2D interface acts as an internal slip barrier, causing mobile and propagating dislocations to disappear or reflect upon encountering the interface, as shown in Fig. 23(c–e). For M-C_{60}/Cu (Embedding), the intrinsic elasticity and discontinuous surface lead to more dislocation annihilation, resulting in superior plasticity.

4. Conclusions

Through molecular dynamics simulations, 2D/metal composite models were established to elucidate the reinforcement mechanisms of monolayer fullerene (M-C_{60}) and graphene in copper-based composites. Five fundamental advances emerge from systematic nanoindentation simulations:

(1) M-C_{60}/Cu composites exhibit superior mechanical performance across configurations and conditions. Surface coatings boost hardness by up to 24.2% via dislocation multiplication and carbon-chain formation, while embedded structures maximize ductility (Pugh ratio $\approx$ 3.48) by absorbing and reflecting dislocations.
(2) Compared to graphene, M-C_{60} exhibits higher interfacial bonding site density (26.3%), mechanical interlocking via fullerene cages, and superior stress-buffering, explaining its greater strengthening and ductility-tuning versatility.
(3) At high strain rates, M-C_{60}/Cu retains hardness by resisting brittle fracture and sustaining dislocation loop formation, unlike graphene coatings that fail catastrophically.
(4) Under elevated temperatures, M-C_{60}/Cu uniquely maintains or increases dislocation density due to strong Cu–C bonding and rough surface morphology, whereas Gr/Cu softens through dislocation annihilation and reduced twinning.
(5) Although the indenter geometry can affect the magnitude of load drop and the contact stiffness, the hardness enhancement and dislocation-blocking advantages of M-C_{60} remain robust across different indenter shapes.

Although the present work is based on high-rate atomistic simulations and experimental fabrication of M-C_{60}/Cu remains challenging, the mechanistic trends are robust and likely to persist in practical applications. The demonstrated ability of M-C_{60} to outperform graphene in both high-strain-rate and high-temperature regimes highlights its potential for aerospace, microelectronic, and other extreme-environment applications. This study provides a predictive framework for designing next-generation metal matrix composites that overcome the conventional strength-ductility trade-off through rational 2D/metal interface engineering.

CRediT authorship contribution statement

Qing Peng: Writing – review & editing, Supervision, Funding acquisition, Formal analysis, Conceptualization, Writing – original draft. **Yuqiang Zhang:** Writing – original draft, Data curation, Conceptualization, Formal analysis, Writing – review & editing. **Gen Chen:** Software, Methodology. **Zeyu Huang:** Software, Methodology. **Xintian Cai:** Writing – review & editing. **Wenhan Zeng:** Writing – review & editing. **Wenbin Zhong:** Writing – review & editing. **Zhongwei Hu:** Supervision, Funding acquisition. **Xiao-Jia Chen:** Writing – review & editing. **Xiangqian Jiang:** Supervision, Project administration.

Declaration of competing interest

The authors declare that they have no known competing financial interests or personal relationships that could have appeared to influence the work reported in this paper.

Acknowledgments

This research was funded by the National Natural Science Foundation of China (Grant No. 12272378, T2527901, 52175404), Strategic Priority Research Program of Chinese Academy of Sciences (Grant No. XDB0620103), Shenzhen Science and Technology Program (Grant No. KQTD20200820113045081), Doctoral Scientific Research Start-up Foundation of Hubei University of Technology (Grant No. XJ2024008301), Educational Commission of Hubei Province of China (Grant No. Q20233005), and the UK's EPSRC funding of Future Metrology Hub (Ref: EP/P006930/1).

Appendix A. Supplementary data

Supplementary data to this article can be found online at https://doi.org/10.1016/j.msea.2026.149883.

Data availability

Data will be made available on request.

References

[1] J. Hou, B. Deng, H. Zhu, et al., Magic auxeticity angle of graphene, Carbon 149 (2019) 350–354, https://doi.org/10.1016/j.carbon.2019.04.057.
[2] Q. Cao, X. Geng, H. Wang, et al., A review of current development of graphene mechanics, Crystals 8 (9) (2018) 357, https://doi.org/10.3390/cryst8090357.
[3] M. Liu, C. Zhang, A. Han, et al., Modulation of morphology and electronic structure on MoS_2-based electrocatalysts for water splitting, Nano Res. 15 (8) (2022) 6862–6887, https://doi.org/10.1021/acsomega.3c02623.
[4] Q. Peng, S. De, Outstanding mechanical properties of monolayer MoS2 and its application in elastic energy storage, Phys. Chem. Chem. Phys. 15 (44) (2013) 19427–19437, https://doi.org/10.1039/C3CP52879K.
[5] R. Maheswaran, B.P. Shanmugavel, A critical review of the role of carbon nanotubes in the progress of next-generation electronic applications, J. Electron. Mater. 51 (6) (2022) 2786–2800, https://doi.org/10.1007/s11664-022-09516-8.
[6] S. Liu, L. Xie, Q. Peng, et al., Carbon nanotubes enhance the radiation resistance of bcc iron revealed by atomistic study, Materials 12 (2) (2019) 217, https://doi.org/10.3390/ma12020217.
[7] K. Khan, A.K. Tareen, M. Aslam, et al., Recent developments in emerging two-dimensional materials and their applications, J. Mater. Chem. C 8 (2) (2020) 387–440, https://doi.org/10.1039/C9TC04187G.
[8] L. Hou, X. Cui, B. Guan, et al., Synthesis of a monolayer fullerene network, Nature 606 (7914) (2022) 507–510, https://doi.org/10.1038/s41586-022-04771-5.
[9] F. Yuan, W. Su, F. Gao, Monolayer 2D polymeric fullerene: a new member of the carbon material family, Chem 8 (8) (2022) 2079–2081, https://doi.org/10.1016/j.chempr.2022.07.008.
[10] E. Meirzadeh, A.M. Evans, M. Rezaee, et al., A few-layer covalent network of fullerenes, Nature 613 (7942) (2023) 71–76, https://doi.org/10.1038/s41586-022-05401-w.
[11] B. Mortazavi, X. Zhuang, Low and anisotropic tensile strength and thermal conductivity in the single-layer fullerene network predicted by machine-learning interatomic potentials, Coatings 12 (8) (2022) 1171, https://doi.org/10.3390/coatings12081171.
[12] P. Ying, Z. Zhong, J. Zhang, Anisotropic mechanical properties of monolayer fullerene network: an interplay between two types of interfullerene bonds. https://doi51.org/10.26434/chemrxiv-2022-kgxfk, 2022.
[13] R.M. Tromer, L.A.R. Junior, D.S. Galvão, A DFT study of the electronic, optical, and mechanical properties of a recently synthesized monolayer fullerene network, Chem. Phys. Lett. 804 (2022) 139925, https://doi.org/10.1016/j.cplett.2022.139925.
[14] B. Peng, Monolayer fullerene networks as photocatalysts for overall water splitting, J. Am. Chem. Soc. 144 (43) (2022) 19921–19931, https://doi.org/10.1021/jacs.2c08054.
[15] Q. Peng, W. Ji, S. De, Mechanical properties of graphene monolayers: a first-principles study, Phys. Chem. Chem. Phys. 14 (38) (2012) 13385–13391, https://doi.org/10.1039/C2CP42387A.

[16] M.A. Rafiee, J. Rafiee, Z. Wang, et al., Enhanced mechanical properties of nanocomposites at low graphene content, ACS Nano 3 (12) (2009) 3884–3890, https://doi.org/10.1021/nn9010472.
[17] Y. Zhang, Y. Wang, C.M. Wang, et al., Thermal conductivity of graphene and its polymer nanocomposites: a review, Adv. Computat. Nanomech. (2016) 1–28, https://doi.org/10.1002/9781119068921.ch1.
[18] Y. Li, S. Wang, Q. Wang, A molecular dynamics simulation study on enhancement of mechanical and tribological properties of polymer composites by introduction of graphene, Carbon 111 (2017) 538–545, https://doi.org/10.1016/j.carbon.2016.10.039.
[19] J.Q. Zhu, X. Liu, Q.S. Yang, Dislocation-blocking mechanism for the strengthening and toughening of laminated graphene/Al composites, Comput. Mater. Sci. 160 (2019) 72–81, https://doi.org/10.1016/j.commatsci.2018.12.061.
[20] J. Zhu, X. Liu, X. Zhou, et al., Strengthening effect of graphene-edge dislocation interaction in graphene reinforced copper matrix composites, Comput. Mater. Sci. 188 (2021) 110179, https://doi.org/10.1016/j.commatsci.2020.110179.
[21] A. Montazeri, A. Mobarghei, Nanotribological behavior analysis of graphene/metal nanocomposites via MD simulations: new concepts and underlying mechanisms, J. Phys. Chem. Solid. 115 (2018) 49–58, https://doi.org/10.1016/j.jpcs.2017.12.012.
[22] Y. Kim, J. Lee, M.S. Yeom, et al., Strengthening effect of single-atomic-layer graphene in metal–graphene nanolayered composites, Nat. Commun. 4 (1) (2013) 2114, https://doi.org/10.1038/ncomms3114.
[23] C. Zhang, C. Lu, G. Michal, et al., Strong strain hardening in graphene/nanotwinned metal composites revealed by molecular dynamics simulations, Int. J. Mech. Sci. 201 (2021) 106460, https://doi.org/10.1016/j.ijmecsci.2021.106460.
[24] S.M. Turkane, A.K. Kureshi, Emerging interconnects: a state-of-the-art review and emerging solutions, Int. J. Electron. 104 (7) (2017) 1107–1119, https://doi.org/10.1080/00207217.2017.1285436.
[25] Y.L. Cheng, C.Y. Lee, Y.L. Huang, Copper metal for semiconductor interconnects [J]. Noble and precious metals-properties, Nanoscale Effects Appl. (2018) 220–221, https://doi.org/10.5772/intechopen.72396.
[26] J.Z. Huang, P.C. Tsao, E.C. Chang, et al., Improving the electromigration life of advanced interconnects through graphene capping, ACS Appl. Nano Mater. (2023), https://doi.org/10.1021/acsanm.3c02055.
[27] S. Mukesh, N.A. Lanzillo, A multiscale simulation study of the structural integrity of damascene interconnects in advanced technology nodes, IEEE Trans. Electron. Dev. 70 (4) (2023) 1977–1982, https://doi.org/10.1109/TED.2023.3242632.
[28] M. Hammad, J.J. Adjizian, C.H. Sacré, et al., Adhesionless and near-ideal contact behavior of graphene on Cu thin film, Carbon 122 (2017) 446–450, https://doi.org/10.1016/j.carbon.2017.06.037.
[29] F. Shuang, K.E. Aifantis, Dislocation-graphene interactions in Cu/graphene composites and the effect of boundary conditions: a molecular dynamics study, Carbon 172 (2021) 50–70, https://doi.org/10.1016/j.carbon.2020.09.043.
[30] L. Yu, J. Xu, B. Peng, et al., Anisotropic optical, mechanical, and thermoelectric properties of two-dimensional fullerene networks, J. Phys. Chem. Lett. 13 (50) (2022) 11622–11629, https://doi.org/10.1021/acs.jpclett.2c02702.
[31] Z. Li, Y. Chen, Z. Li, et al., Thermal property of fullerene fibers: one-dimensional material with exceptional thermal performance, Small 20 (22) (2024) 2307671, https://doi.org/10.1002/smll.202307671.
[32] P. Ying, H. Dong, T. Liang, et al., Atomistic insights into the mechanical anisotropy and fragility of monolayer fullerene networks using quantum mechanical calculations and machine-learning molecular dynamics simulations, Extreme Mech. Lett. 58 (2023) 101929, https://doi.org/10.1016/j.eml.2022.101929.
[33] G. Shen, L. Li, S. Tang, et al., Stability and elasticity of quasi-hexagonal fullerene monolayer from first-principles study, Crystals 13 (2) (2023) 224, https://doi.org/10.3390/cryst13020224.
[34] L.A.R. Junior, M.L.P. Junior, W.F. Giozza, et al., Thermal stability and fracture patterns of a recently synthesized monolayer fullerene network: a reactive molecular dynamics study, Chem. Phys. Lett. 807 (2022) 140075, https://doi.org/10.1016/j.cplett.2022.140075.
[35] B. Peng, Stability and strength of monolayer polymeric C_{60}, Nano Lett. 23 (2) (2023) 652–658, https://doi.org/10.1021/acs.nanolett.2c04497.
[36] J. Choi, A review of the mechanical design of materials based on molecular dynamics simulations, Multiscale Sci. Eng. 5 (3) (2023) 86–103, https://doi.org/10.1007/s42493-024-00105-x.
[37] Y. Zhang, Z. Hu, Y. Chen, et al., Insights into scratching force in axial ultrasonic vibration-assisted single grain scratching, J. Manuf. Process. 112 (2024) 150–160, https://doi.org/10.1016/j.jmapro.2024.01.005.
[38] L. Li, Y. Zhang, L. Xiong, et al., Strengthening effect of shear-induced wrinkles on graphene/copper nanocomposites by an atomistic investigation, J. Alloys Compd. (2024) 175291, https://doi.org/10.1016/j.jallcom.2024.175291.
[39] P. Wang, Q. Cao, H. Wang, et al., Fivefold enhancement of yield and toughness of copper nanowires via coating carbon nanotubes, Nanotechnology 31 (11) (2019) 115703, https://doi.org/10.1088/1361-6528/ab5cd7.
[40] W. Peng, K. Sun, Effects of Cu/graphene interface on the mechanical properties of multilayer Cu/graphene composites, Mech. Mater. 141 (2020) 103270, https://doi.org/10.1016/j.mechmat.2019.103270.
[41] P. Wang, Q. Cao, Y. Lan, et al., Nanostructuring enforced sandwich-tubular CNT-Cu interconnects, Compos. Struct. 278 (2021) 114705, https://doi.org/10.1016/j.compstruct.2021.114705.
[42] S. Weng, H. Ning, T. Fu, et al., Molecular dynamics study of strengthening mechanism of nanolaminated graphene/Cu composites under compression, Sci. Rep. 8 (1) (2018) 3089, https://doi.org/10.1038/s41598-018-21390-1.
[43] S. Plimpton, Fast parallel algorithms for short-range molecular dynamics, J. Comput. Phys. 117 (1) (1995) 1–19, https://doi.org/10.1006/jcph.1995.1039.
[44] C. Zhang, C. Lu, L. Pei, et al., The negative Poisson's ratio and strengthening mechanism of nanolayered graphene/Cu composites, Carbon 143 (2019) 125–137, https://doi.org/10.1016/j.carbon.2018.10.097.
[45] H. Zheng, Z.F. Wang, T. Luo, et al., Analytical study of electronic structure in armchair graphene nanoribbons, Phys. Rev. B 75 (16) (2007) 165414, https://doi.org/10.1103/PhysRevB.75.165414.
[46] X. Zhou, X. Liu, J. Lei, et al., Atomic simulations of the formation of twist grain boundary and mechanical properties of graphene/aluminum nanolaminated composites, Comput. Mater. Sci. 172 (2020) 109342, https://doi.org/10.1016/j.commatsci.2019.109342.
[47] S. Norouzi, M.M.S. Fakhrabadi, Anisotropic nature of thermal conductivity in graphene spirals revealed by molecular dynamics simulations, J. Phys. Chem. Solid. 137 (2020) 109228, https://doi.org/10.1016/j.jpcs.2019.109228.
[48] W. Peng, K. Sun, M. Zhang, et al., Effects of graphene coating on the plastic deformation of single crystal copper nano-cuboid under different nanoindentation modes, Mater. Chem. Phys. 225 (2019) 1–7, https://doi.org/10.1016/j.matchemphys.2018.12.028.
[49] S.M. Foiles, M.I. Baskes, M.S. Daw, Embedded-atom-method functions for the fcc metals Cu, Ag, Au, Ni, Pd, Pt, and their alloys, Phys. Rev. B 33 (12) (1986) 7983, https://doi.org/10.1103/PhysRevB.33.7983.
[50] X. Zhu, Y. Zhao, L. Ma, et al., Graphene coating makes copper more resistant to plastic deformation, Compos. Commun. 12 (2019) 106–111, https://doi.org/10.1016/j.coco.2019.01.006.
[51] Y. Zhao, X. Peng, T. Fu, et al., Strengthening mechanisms of graphene coated copper under nanoindentation, Comput. Mater. Sci. 144 (2018) 42–49, https://doi.org/10.1016/j.commatsci.2017.12.009.
[52] J. Li, Q. Fang, Y. Liu, et al., A molecular dynamics investigation into the mechanisms of subsurface damage and material removal of monocrystalline copper subjected to nanoscale high speed grinding, Appl. Surf. Sci. 303 (2014) 331–343, https://doi.org/10.1016/j.apsusc.2014.02.178.
[53] W. Wang, Q. Peng, Y. Dai, et al., Distinctive nanofriction of graphene coated copper foil, Comput. Mater. Sci. 117 (2016) 406–411, https://doi.org/10.1016/j.commatsci.2016.01.007.
[54] H. Xie, Z. Ma, W. Zhang, et al., Probing the atomic-scale origins of anti-friction and wear-resisting in graphene-coated high-entropy alloys, Mater. Des. 223 (2022) 111178, https://doi.org/10.1016/j.matdes.2022.111178.
[55] A. Stukowski, Visualization and analysis of atomistic simulation data with OVITO–the Open Visualization Tool, Model. Simulat. Mater. Sci. Eng. 18 (1) (2009) 015012, https://doi.org/10.1088/0965-0393/18/1/015012.
[56] A. Stukowski, V.V. Bulatov, A. Arsenlis, Automated identification and indexing of dislocations in crystal interfaces, Model. Simulat. Mater. Sci. Eng. 20 (8) (2012) 085007, https://doi.org/10.1088/0965-0393/20/8/085007.
[57] Giovanni Bussi, Tanya Timan, Isothermal-isobaric molecular dynamics using stochastic velocity rescaling, J. Chem. Phys. 130 (7) (2009) 074101, https://doi.org/10.1063/1.3073889.
[58] J. Lin, F. Jiang, Q. Wen, et al., Deformation anisotropy of scratching on C-plane of sapphire: a molecular dynamics study and experiment, Appl. Surf. Sci. 546 (2021) 149091, https://doi.org/10.1016/j.apsusc.2021.149091.
[59] S. Zhao, X. Zhang, Y. Ni, et al., Anisotropic mechanical response of a 2D covalently bound fullerene lattice, Carbon 202 (2023) 118–124, https://doi.org/10.1016/j.carbon.2022.11.005.
[60] W. Li, R. Yang, M. Sun, Superior thermoelectric properties of bulk and monolayer fullerene networks, J. Mater. Chem. A 11 (8) (2023) 3949–3960, https://doi.org/10.1039/D2TA08537B.
[61] W. Li, M. Sun, Electronic band structure and anisotropic optical properties of bulk and monolayer fullerene networks, Spectrochim. Acta Mol. Biomol. Spectrosc. 298 (2023) 122756, https://doi.org/10.1016/j.saa.2023.122756.
[62] T. Zhang, X. Li, H. Gao, Fracture of graphene: a review, Int. J. Fract. 196 (2015) 1–31, https://doi.org/10.1007/s10704-015-0039-9.
[63] L. Li, X. Sun, Y. Guo, et al., Nanoindentation response of monocrystalline copper under various tensile pre-deformations via molecular dynamic simulations, Adv. Mech. Eng. 10 (12) (2018), https://doi.org/10.1177/1687814018816874.
[64] Hertz, Ueber die Berührung fester elastischer Körper, J.die reine Angew. Math. Crelle's J. (1882) 156, https://doi.org/10.1515/crll.1882.92.156.
[65] T.S. Vashakmadze, The Theory of Anisotropic Elastic Plates[M], Springer Science & Business Media, 2013.
[66] W. Yu, A unified theory for constitutive modeling of composites, J. Mech. Mater. Struct. 11 (4) (2016) 379–411, https://doi.org/10.2140/jomms.2016.11.379.
[67] D.L. Tian, X.P. Zhou, A continuum-kinematics-inspired peridynamic model of anisotropic continua: elasticity, damage, and fracture, Int. J. Mech. Sci. 199 (2021) 106413, https://doi.org/10.1016/j.ijmecsci.2021.106413.
[68] Z. Zheng, K. Huang, C. Lin, et al., Fundamental investigation on damage evolution and material removal mechanism in scratching anisotropic brittle material, Tribol. Int. 197 (2024) 109764, https://doi.org/10.1016/j.triboint.2024.109764.
[69] G.J. Olguín-Orellana, J.A. de la Rosa Abad, M.B. Camarada, et al., On the mechanical response of graphene-capped copper nanoparticles, Phys. Chem. Chem. Phys. 26 (3) (2024) 2260–2268, https://doi.org/10.1021/acs.jpcc.3c04029.
[70] A.B. Shinde, A. Owhal, A. Sharma, et al., Comparative analysis of mechanical properties for mono and poly-crystalline copper under nanoindentation–insights from molecular dynamics simulations, Mater. Chem. Phys. 277 (2022) 125559, https://doi.org/10.1016/j.matchemphys.2021.125559.
[71] W.C. Oliver, G.M. Pharr, An improved technique for determining hardness and elastic modulus using load and displacement sensing indentation experiments, J. Mater. Res. 7 (6) (1992) 1564–1583, https://doi.org/10.1557/JMR.1992.156.

[72] C. Lu, Y.W. Mai, P.L. Tam, et al., Nanoindentation-induced elastic–plastic transition and size effect in α-Al_2O_3 (0001), Philos. Mag. Lett. 87 (6) (2007) 409–415, https://doi.org/10.1080/09500830701203156.
[73] Q. Huimin, L. Yang, Y. Jiaxin, et al., Role of fullerene carbon on tribological performance of polyimide composites at a large temperature span, Tribol. Int. 173 (2022) 107628, https://doi.org/10.1016/j.triboint.2022.107628.
[74] M.F. Doerner, W.D. Nix, A method for interpreting the data from depth-sensing indentation, J. Mater. Res. 1 (1986) 4.
[75] P. Haušild, J. Čech, B. Merle, et al., Effect of temperature and strain rate on indentation size effect at shallow indentation depths, Mater. Des. (2025) 114196, https://doi.org/10.1016/j.matdes.2025.114196.
[76] P. Fan, N.K. Katiyar, M. Arshad, et al., Anisotropic plasticity mechanisms in a newly synthesized high entropy alloy investigated using atomic simulations and nanoindentation experiments, J. Alloys Compd. 970 (2024) 172541, https://doi.org/10.1016/j.jallcom.2023.172541.
[77] T. Paulauskas, C. Buurma, E. Colegrove, et al., Atomic scale study of polar Lomer–Cottrell and Hirth lock dislocation cores in CdTe, Acta Crystallogr. A: Foundations Adv. 70 (6) (2014) 524–531, https://doi.org/10.1107/S2053273314019639.
[78] U.F. Kocks, A.S. Argon, M.F. Ashby, Thermodynamics and kinetics of slip, in: B. Chalmers, J.W. Christian, T.B. Massalski (Eds.), Progress in Materials Science, Pergamon Press, Oxford, 1975, p. 4.
[79] P.M. Anderson, J.P. Hirth, J. Lothe, Theory of Dislocations[M], Cambridge University Press, 2017.
[80] Z.Y. Liang, G.M. Pharr, Decoupling indentation size and strain rate effects during nanoindentation: a case study in tungsten, J. Mech. Phys. Solid. 165 (2022) 104935, https://doi.org/10.1016/j.jmps.2022.104935.
[81] G.I. Taylor, The mechanism of plastic deformation of crystals. Part I.—Theoretical, Proc. R. Soc. Lond. - Ser. A Contain. Pap. a Math. Phys. Character 145 (855) (1934) 362–387.
[82] Q. Tang, J. Li, B.C. Hornbuckle, et al., Suppressed ballistic transport of dislocations at strain rates up to 109 s–1 in a stable nanocrystalline alloy, Commun. Mater. 6 (1) (2025) 43, https://doi.org/10.1038/s43246-025-00757-8.
[83] D. Hull, D.J. Bacon, Introduction to Dislocations[M], Elsevier, 2011.
[84] X. Zheng, X. Du, J. Wu, et al., Revealing crack resistance in gradient nano-grained CoCrFeMnNi high-entropy alloys: a molecular dynamics study, Int. J. Plast. 191 (2025) 104392, https://doi.org/10.1016/j.ijplas.2025.104392.
[85] H. Fan, Q. Wang, J.A. El-Awady, et al., Strain rate dependency of dislocation plasticity, Nat. Commun. 12 (1) (2021) 1845, https://doi.org/10.1038/s41467-021-21939-1.
[86] B. Grabowski, N. Zotov, Thermally-activated dislocation mobility in bcc metals: an accelerated molecular dynamics study, Comput. Mater. Sci. 200 (2021) 110804, https://doi.org/10.1016/j.commatsci.2021.110804.
[87] A. Banerjee, S. Dhar, S. Acharyya, et al., Determination of Johnson cook material and failure model constants and numerical modelling of Charpy impact test of armour steel, Mater. Sci. Eng., A 640 (2015) 200–209, https://doi.org/10.1016/j.msea.2015.05.073.
[88] B.C. De Cooman, Y. Estrin, S.K. Kim, Twinning-induced plasticity (TWIP) steels, Acta Mater. 142 (2018) 283–362, https://doi.org/10.1016/j.actamat.2017.06.046.
[89] J. Huang, Y. Liu, X. Yu, et al., Nano mechanical property analysis of single crystal copper using Berkovich nano indenter and molecular dynamic simulation, Comput. Mater. Sci. 188 (2021) 110237, https://doi.org/10.1016/j.commatsci.2020.110237.